

## Measurements of elastic electron-proton scattering at large momentum transfer

A. F. Sill,\* R. G. Arnold, P. E. Bosted, C. C. Chang,<sup>†</sup> J. Gomez,<sup>‡</sup> A. T. Katramatou,  
C. J. Martoff,<sup>§</sup> G. G. Petratos,\*\* A. A. Rahbar, S. E. Rock, and Z. M. Szalata  
*Department of Physics, The American University, Washington, D.C. 20016*

D. J. Sherden

*Stanford Linear Accelerator Center, Stanford University, Stanford, California 94309*

J. M. Lambert

*Department of Physics, Georgetown University, Washington, D.C. 20057*

R. M. Lombard-Nelsen

*DAPNIA/SPhN, CE Saclay, Gif-sur-Yvette, 91191 CEDEX, France*

(Received 23 November 1992)

Measurements of the forward-angle differential cross section for elastic electron-proton scattering were made in the range of momentum transfer from  $Q^2=2.9$  to  $31.3$   $(\text{GeV}/c)^2$  using an electron beam at the Stanford Linear Accelerator Center. The data span six orders of magnitude in cross section. Combined statistical and systematic uncertainties in the cross section measurements ranged from 3.6% at low  $Q^2$  to 19% at high  $Q^2$ . These data have been used to extract the proton magnetic form factor  $G_M^p(Q^2)$  and Dirac form factor  $F_1^p(Q^2)$  by using form factor scaling. The logarithmic falloff of  $Q^4 F_1^p$  expected from leading twist predictions of perturbative quantum chromodynamics is consistent with the new data at high  $Q^2$ . Some nonperturbative and hybrid calculations also agree with our results.

PACS number(s): 13.60.Fz, 12.38.Qk, 13.40.Fn

### I. INTRODUCTION

This paper reports measurements of the cross section for elastic electron scattering from protons that significantly improve the precision compared to previous data at large values of four-momentum transfer  $q$ . The data are in agreement with previous measurements [1,2] and a subsequent measurement [3] at low-momentum transfer and extend from  $Q^2 \equiv -q^2 = 2.9$  to  $Q^2 = 31.3$   $(\text{GeV}/c)^2$ . With the assumption that the contribution to the cross section of the proton electric form factor  $G_E^p$  is small, as indicated by previous experiments at low  $Q^2$ , these cross-section measurements can be used to extract the proton magnetic form factor  $G_M^p$ , or Dirac form factor  $F_1^p$ , with sufficient precision to allow significant comparisons with the predictions of both perturbative and nonperturbative quantum chromodynamics (QCD). At high-momentum transfer, the results are in agreement with the logarithmic falloff of  $Q^4 F_1^p$  expected from perturbative leading order, leading twist analyses [4–8] of

nucleon form factors. A summary and preliminary results of this experiment have been published in Ref. [9]. Additional details may also be found in Ref. [10]. This paper reports final results after improvements in the radiative corrections and acceptance calculation procedures.

The paper is organized as followed. After a brief review of elastic scattering kinematics, the beam, target, spectrometers, and other equipment are described in Sec. II. The data-acquisition strategy and analysis methods are discussed in Sec. III. Calculation of the elastic electron-proton cross sections and extraction of values for the leading proton form factor (either  $G_M^p$  or  $F_1^p$ ) are contained in Sec. IV, at the end of which the experimental results and a discussion of systematic uncertainties are given. Section V gives a brief summary of the present theoretical situation and compares the results of this experiment with both perturbative and nonperturbative QCD predictions.

#### A. Overview of elastic scattering kinematics

The kinematics of electron-proton scattering are shown schematically in Fig. 1. An electron with initial four-momentum  $e$  scatters from a proton of four-momentum  $p$  and emerges with a final four-momentum  $e'$ . The virtual photon transfers a four-momentum  $q$  to the proton. In the case of elastic scattering,  $(p+q)^2 = (p')^2 = M_p^2$ , where  $M_p$  is the mass of the proton.

In the laboratory frame for a proton initially at rest, the four-momentum transfer squared  $q^2$  is related to the incident energy  $E$ , final energy  $E'$ , and scattering angle  $\theta$  of the electron by the expression  $q^2 = -4EE'\sin^2(\theta/2)$ .

\*Present address: Department of Physics and Astronomy, University of Rochester, Rochester, NY 14627.

<sup>†</sup>Permanent address: Department of Physics and Astronomy, University of Maryland, College Park, MD 20742.

<sup>‡</sup>Present address: Continuous Electron Beam Accelerator Facility, Newport News, VA 23606.

<sup>§</sup>Present address: Temple University, Philadelphia, PA 19122.

\*\*Present address: Stanford Linear Accelerator Center, Stanford, CA 94309.

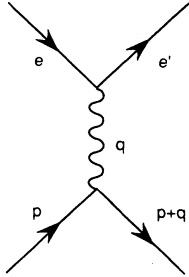


FIG. 1. Kinematics of electron-proton scattering.

It is customary for spacelike processes to refer to the momentum transfer squared as  $Q^2 \equiv -q^2$ , which is a positive quantity.

### 1. Representation of elastic cross section in terms of form factors

The elastic cross section can be represented in terms of the proton magnetic and electric form factors  $G_M^p(Q^2)$  and  $G_E^p(Q^2)$  as

$$\frac{d\sigma}{d\Omega} = \left( \frac{d\sigma}{d\Omega} \right)_{\text{NS}} \left\{ \frac{G_E^2(Q^2) + \tau G_M^2(Q^2)}{1 + \tau} + 2\tau G_M^2(Q^2) \tan^2(\theta/2) \right\}, \quad (1)$$

or in terms of the proton Dirac and Pauli form factors  $F_1^p(Q^2)$  and  $F_2^p(Q^2)$  as

$$\frac{d\sigma}{d\Omega} = \left( \frac{d\sigma}{d\Omega} \right)_{\text{NS}} \left\{ F_1^2(Q^2) + \tau \kappa_p^2 F_2^2(Q^2) + 2\tau [F_1(Q^2) + \kappa_p F_2(Q^2)]^2 \tan^2(\theta/2) \right\}, \quad (2)$$

where  $\tau \equiv Q^2/4M_p^2$ ,  $\kappa_p = \mu_p - 1$  is the anomalous magnetic moment of the proton (1.7928...) and  $(d\sigma/d\Omega)_{\text{NS}}$  is the no-spin, "nonstructure" cross section:

$$\begin{aligned} \left( \frac{d\sigma}{d\Omega} \right)_{\text{NS}} &= \frac{(\alpha \hbar c)^2 \cos^2(\theta/2)}{4E^2 \sin^4(\theta/2) [1 + 2(E/M_p) \sin^2(\theta/2)]} \\ &= \left( \frac{d\sigma}{d\Omega} \right)_{\text{Mott}} \frac{E'}{E}. \end{aligned} \quad (3)$$

The Sachs form factors  $G_E$  and  $G_M$  are related to the Dirac and Pauli form factors  $F_1$  and  $F_2$  by the expressions  $G_M = F_1 + \kappa F_2$  and  $G_E = F_1 - \tau \kappa F_2$ . Here  $F_1$  corresponds to the helicity-conserving part of the cross section, while  $F_2$  corresponds to the helicity flip part. For a pointlike, spin- $\frac{1}{2}$  particle with unit charge and no anomalous magnetic moment,  $F_1 = 1$  and  $F_2 = 0$ .

### 2. Form factor scaling

At low-momentum transfers [ $Q^2 \leq 7$  (GeV/c)<sup>2</sup>],  $G_E^p$  has been found to scale [1,2] with  $G_M^p$  such that

$G_E^p(Q^2) \approx G_M^p(Q^2)/\mu_p$ . In terms of  $F_1$  and  $F_2$ , the form factor scaling relation becomes

$$F_2^p \approx F_1^p / (1 + \mu_p \tau). \quad (4)$$

The electric form factor  $G_E^p$  has not yet been measured with good precision above  $Q^2 \approx 7$  (GeV/c)<sup>2</sup>. If form factor scaling continues, the contribution of  $G_M^p$  to the cross section dominates over that of  $G_E^p$  at high  $Q^2$ . The contribution of  $G_E^p$  to the cross section under this assumption is typically a few percent above  $Q^2 = 5$  (GeV/c)<sup>2</sup>, and so moderate deviations from form factor scaling would have little effect on the extracted value of  $G_M^p$  for most of the data in this experiment. Extraction of the Dirac form factor depends more heavily on the assumption of form factor scaling (see Sec. IV).

## II. EQUIPMENT

The experiment, known as E136, was conducted using the primary electron beam at the Stanford Linear Accelerator Center [11], and the experimental facilities in End Station A. The experimental setup and layout of equipment in End Station A are shown in Fig. 2. The beam was incident on protons in a liquid-hydrogen target. Scattered electrons were detected using the SLAC 8-GeV/c spectrometer. The data reported here are from two experimental runs (E136 I and E136 II) separated by 9 months. There were some differences in equipment and analysis, as described below, but the results were in agreement and have been combined.

### A. Beam and transport system

The accelerator provided electrons with energies from  $E = 5$  to 21.5 GeV in 1.6- $\mu$ sec-long pulses at up to 180 Hz, with typically  $4 \times 10^{11}$  electrons per pulse. Details of the beam transport system have previously been de-

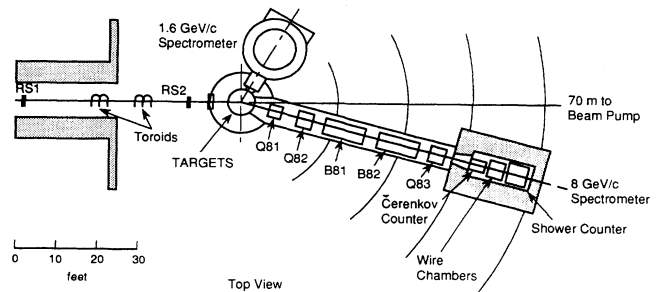


FIG. 2. Experimental setup and layout of equipment in SLAC End Station A. The beam entered from the left and passed through two identical toroidal charge monitors on its way to the targets. The beam position, size, and angle were checked manually by inserting fluorescent screens (RS1 and RS2) every few hours. The beam position and profile were measured continuously with wire arrays, which were part of a computerized beam steering system described in the text. Scattered electrons were detected using the SLAC 8-GeV/c spectrometer. The SLAC 1.6-GeV/c spectrometer was used to monitor the density of the liquid-hydrogen targets.

scribed [12]. The energy spread of the incident beam was limited by slits in the transport system to be typically  $\pm 0.2\%$ . The energy was monitored continuously during the experiment by flip coil measurements of the field in a magnet connected in series with identical magnets in the beam line.

### 1. Toroids

The beam current was measured to within  $\pm 0.5\%$  using two independent charge monitors [13]. Each monitor consisted of a toroidal ferrite core wound with wire to form a current transformer. The coil formed part of a resonant circuit which was excited by the passage of the beam pulse through the toroid. Each signal was analyzed by two sets of electronics which shared a common preamplifier. One set of electronics analyzed the total area of the first positive-going phase of the signal, and the other sampled the signal at a certain optimum point. Each monitor was equipped with a calibration system consisting of a precision capacitor which was charged to a known voltage and then discharged through an additional winding around the toroid. The calibration and zero drift of these systems were checked every few hours, and the zero was adjusted when necessary. After correcting for calibration, the beam charge for experimental data as measured with the two toroids agreed to within  $\pm 0.2\%$  with either set of electronics.

### 2. Beam steering

The beam profile and position in both the horizontal and vertical directions were measured using arrays of thin wires. Some of the early data in this experiment were taken using beam profile monitors which had CuBe wires. Aluminum wires proved less susceptible to warping and distortion due to heating caused by the beam, and were used for the majority of the experiment. Each of these two arrays consisted of a series of 0.13-mm-thick type-1350 Al wires spaced at 0.40 mm intervals. There were 22 wires in each array, providing a total active area of about  $0.8 \text{ (cm)}^2$ . The wire arrays were fixed in the beam line just upstream of the targets, as shown in Fig. 2. The beam-induced secondary emission signals in the wires were read by analogue-to-digital converters (ADC's) connected to a dedicated microprocessor. The microprocessor calculated the beam centroid and width in each direction and kept the beam steered to the desired location at the target to within typically  $\pm 1 \text{ mm}$  by adjusting the current in small trim coils on the windings of the final steering magnets. In order to obtain optimum momentum resolution in the spectrometer, the vertical beam height was kept small [typically 1 mm full width at half maximum (FWHM)]. The width of the beam was typically 2–3 mm FWHM.

The angle of the incident beam was checked every few hours by observing the locations of the beam spots on two ZnS screens upstream of the target. When necessary, the beam angle was adjusted manually by making small changes to the fields in the final steering magnets. The screens were separated by about 10 m and the centroid of the beam could be read to within  $\pm 1 \text{ mm}$ , producing an

uncertainty on the incident angle of the beam of approximately  $\pm 0.2 \text{ mrad}$ .

## B. Targets

### 1. Target construction

Two liquid-hydrogen targets [14] of different lengths were used, along with corresponding empty cells and a set of thin aluminum targets. The target assembly is shown in Fig. 3. A target 25 cm in length was used to determine the normalization of the acceptance for a longer 65-cm target, and for tests at low  $Q^2$ . The long target provided a higher counting rate than the short target and was used to take the majority of the elastic data. The long target was designed to yield the maximum possible counting rate by completely filling the spectrometer acceptance for the angular range of interest. The length of the short target was chosen to allow it to be completely visible within the apertures of the spectrometer for a restricted range of the kinematic variables of the scattered particles. Aluminum targets were used in various tests and in studies of the optics of the spectrometer.

The target cells were constructed as cylinders with axes oriented along the beam direction in order to present the maximum amount of hydrogen to the beam, within the acceptance of the spectrometer, while minimizing the amount of material through which the scattered electrons would pass. The cells contained liquid hydrogen at an average temperature of about 21 K and a cell pressure of approximately 2 atm. Target liquid temperatures were measured with hydrogen vapor pressure bulbs and platinum resistors. The targets were housed in a large vacuum tank which was maintained at a pressure of about  $10^{-7} \text{ Torr}$ . Each cell had an outer diameter of 6.7 cm. Hydrogen flowed in the direction of the beam through an inner cylinder approximately 5 cm in diameter, and out through the annulus between the inner cylinder and cell wall.

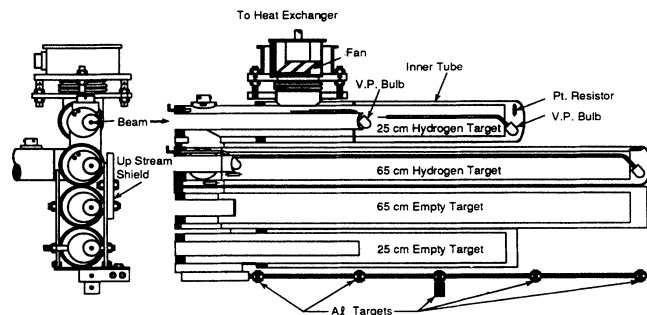


FIG. 3. Liquid-hydrogen and aluminum target assemblies. Liquid hydrogen flowed in the direction of the beam through an inner cylinder and returned in the opposite direction in the outer region of the full targets. Empty target cells of the same length as the hydrogen cells, but with thicker end caps, were used to study the counting rate due to the ends and walls of the targets. Vapor pressure bulbs and platinum resistors used to measure target liquid temperatures are shown. Aluminum targets at various locations along the beam direction were useful in checkout and in tests of the optics of the spectrometer.

The target construction differed for the two parts of the experiment. The first target was built using 0.05- and 0.25-mm Mylar for the inner cylinders and outer walls. This target ruptured after the equivalent of about 100 h of the full-intensity beam, due to the effect of radiation damage to the Mylar walls [14]. The target was then rebuilt with 0.025-mm aluminum inner flow cylinders and 0.125-mm aluminum walls. The second target was used for the remaining 600 h of the experiment. Further details on the composition and dimensions of the target components for the two parts of the experiment are given in Table I.

Because of Fermi smearing, the cross section for inelastic scattering from aluminum in the kinematic region of the hydrogen elastic peak can be substantially larger than for quasielastic scattering from the protons and neutrons in the aluminum nuclei. Since the counting rate for elastic electron-proton scattering was as low as roughly one event per day, special measures were taken to remove the source of potential background counts from the Al end caps. Two tungsten shields were used to prevent particles which scattered from the end caps of the long target from entering the spectrometer. The placement of these shields is illustrated in Fig. 4. The up stream shield was approximately 1.7 cm thick and the down stream shield was approximately 1.4 cm thick. As some previous experiments [1,2] had been troubled by substantial counting rates due to scattering from the entrance and exit windows of the target cells, this design represented a significant improvement in experimental technique. The shields did not affect the visible length of the short target,

but restricted the fraction of the long target that was visible by the spectrometer. The effective length of the long target was determined by comparison to the short target using a procedure described below.

## 2. Circulation and density measurements

The liquid hydrogen in the target cells was circulated through a heat exchanger cooled with liquid hydrogen to remove the heat deposited by the beam. The average target temperature was measured at both ends of each cell using both platinum resistance probes and vapor pressure bulbs. The results of these two methods generally agreed to within  $\pm 0.1\%$ . Temperature rise along the entire length of the long target was typically less than 0.5 K; the average of the temperature measurements at each end was used to calculate the density. The targets were tested thoroughly to check for possible local boiling of the liquid hydrogen due to heat deposited by the beam. The long target used in the first part of the experiment, with which only a small portion of the data used in the analysis were taken, showed a definite effect of local density changes that correlated with beam power, as described below. The targets were redesigned for the second part of the experiment to eliminate this problem.

(a) *Target density tests, E136 I.* In the early part of the experiment, a single vaneaxial fan was used to pump the liquid hydrogen through the target cells. The beam deposited a maximum of roughly 250 W of power in the long hydrogen target. The hydrogen flow rate as calculated from the average temperature rise along the long

TABLE I. Composition and dimensions of various components of the liquid-hydrogen and aluminum target assembly. Dimensions are given at 21 K after allowing for shrinkage. Differences between parts I and II of the experiment are described in the text. The material before the target includes the wire arrays and thin Al vacuum windows, and after the target includes Al vacuum windows and target insulation (aluminized Mylar).

Component (Material)	Length	
	Short target	Long target
E136 I		
Material: Before target=0.0128 r.l. After target=0.0108 r.l.		
Liquid hydrogen	25.36 cm	66.03 cm
Internal tube (Mylar)	0.05 mm	0.05 mm
Side wall (Mylar)	0.25 mm	0.25 mm
Material: Before target=0.0055 r.l. After target=0.0085 r.l.		
Liquid hydrogen	25.04 cm	64.75 cm
Internal tube (Al)	0.025 mm	0.025 mm
Side wall (Al)	0.125 mm	0.125 mm
E136 I and E136 II		
Hydrogen targets		
Upstream end cap (Al)	0.064 mm	0.064 mm
Downstream end cap (Al)	0.127 mm	0.127 mm
Empty targets		
Upstream end cap (Al)	1.27 mm	3.30 mm
Downstream end cap (Al)	1.27 mm	3.30 mm

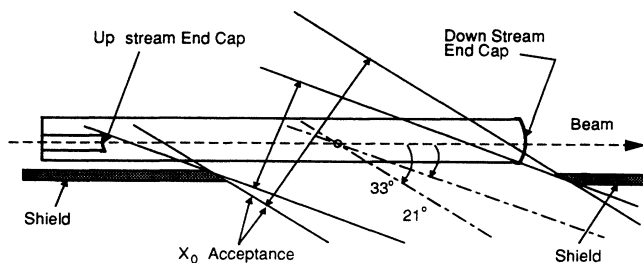


FIG. 4. Placement of tungsten shielding which blocked the long target end caps from the field of view of the spectrometer. A top view of the long hydrogen target and shields is shown. The beam did not pass through the geometrical center of the target, but was offset slightly in the direction of the spectrometers in order to reduce the amount of hydrogen through which the scattered electrons passed. The dot near the center of the target indicates the pivot point about which the spectrometers rotated, as shown in Fig. 2. The location of the central axis of the 8-GeV/c spectrometer is shown for central spectrometer angles of 21° and 33°, and the projected target length seen by the spectrometer at each angle is indicated.

target [14] was roughly 20 cm/sec. Under these conditions, the counting rate for the long target was observed to decrease with increasing beam power by more than would be expected from measured average temperature changes. We attribute this decrease in counting rate to local boiling in the immediate vicinity of the beam. Counting rates for the short target were not affected. Effects were observed in the long target which correlated with changes in the instantaneous beam current, pulse rate, and beam spot size. All elastic data used in the analysis were taken under similar conditions in these variables.

A target density correction to the cross sections from the long target was determined by comparing short and long target elastic data at low-momentum transfer, as shown in Table II. Cross-section measurements for data taken with the long and short targets at  $Q^2=5$  (GeV/c)<sup>2</sup>

and  $Q^2=12$  (GeV/c)<sup>2</sup> were compared and the resulting correction factor of  $1.06\pm 0.02$  was applied to the data for the long target at  $Q^2=31$  (GeV/c)<sup>2</sup>. This is considerably smaller than the statistical error on this kinematic point. Cross sections measured with the short target in E136 I agreed with those measured with either target during E136 II. Approximately 40% of the data at  $Q^2=31.3$  (GeV/c)<sup>2</sup> were affected by the target density correction.

The SLAC 1.6-GeV/c spectrometer was also used as a relative density monitor by setting it to detect recoil protons from  $e$ - $p$  elastic scattering at kinematics that provided a high counting rate. The counting rates in the 1.6-GeV/c spectrometer were found to be more sensitive to the beam halo and other backgrounds than those in the 8-GeV/c spectrometer. No correction was ever applied to the data based solely on data from the 1.6-GeV/c spectrometer. Nonetheless these data provided a useful means of checking for possible target density changes since the counting rates in the 8-GeV/c spectrometer during the high- $Q^2$  elastic measurements were generally quite low.

(b) *Target changes and density tests, E136 II.* The hydrogen flow was more than quadrupled for the second part of the experiment by streamlining the manifold and replacing the single circulating fan with two larger fans [15]. The results of tests of density dependence on target circulation after this change are shown in Fig. 5. The pulse rate never exceeded 120 Hz during the second part of the experiment due to accelerator limitations. Local density changes were unmeasurable (less than 1%) under these conditions even with one circulating fan off and the other at half speed. Both fans were operated at full speed during the normal course of the experiment, providing substantially increased cooling capacity over the conditions of the test shown in Fig. 5. Local target boiling was thus not a problem for the majority of the experiment. The resulting systematic uncertainty in target density was estimated as less than  $\pm 1.0\%$  for the combined  $Q^2=31.3$  (GeV/c)<sup>2</sup> data sets, and  $\pm 0.5\%$  for all other data.

TABLE II. Comparison of elastic cross sections from the short ( $S$ ) and long ( $L$ ) targets used to determine the density correction due to beam heating in the long target during part I of the experiment. The density correction was correlated with average beam current (product of pulse rate and peak current) and spot size. Spot size here means the product of the average FWHM horizontal and vertical beam distributions as measured by the wire arrays.

Target	$Q^2$ [(GeV/c) <sup>2</sup> ]	Pulse rate (Hz)	$\langle I \rangle_{\text{peak}}$ (mA)	Spot size (mm <sup>2</sup> )	$d\sigma/d\Omega$ (nb/sr)	$\frac{(d\sigma/d\Omega)_S}{(d\sigma/d\Omega)_L}$
Short	5.0	160	32	3.4	$(6.84\pm 0.04)\times 10^{-2}$	
Long	5.0	120	36	2.6	$(6.50\pm 0.04)\times 10^{-2}$	$1.05\pm 0.01$
Short	5.0	140	40	$\sim 1$	$(2.01\pm 0.04)\times 10^{-2}$	
Long	5.0	160	40	$\sim 1$	$(1.90\pm 0.04)\times 10^{-2}$	$1.06\pm 0.03$
Short	12.0	140	45	4.3	$(7.92\pm 0.30)\times 10^{-4}$	
Long	12.0	160	40	2.9	$(7.53\pm 0.18)\times 10^{-4}$	$1.05\pm 0.04$

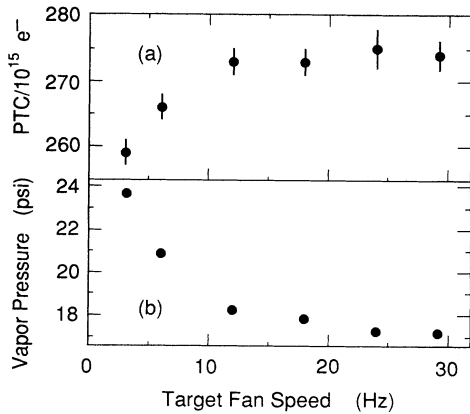


FIG. 5. Dependence of the counting rate on target circulation for inelastic data taken with the long target in E136 II. The abscissa is the rotational speed of one of the circulating fans used to pump the liquid through the cells. The other identical fan caps were turned off for this test. The ordinate shows (a) the counting rate for electrons, where PTC is the threefold coincidence of the PR, TA, and CC; and (b) the vapor pressure at the downstream end of the long hydrogen target. Local density changes in the hydrogen were less than 1%, even with one fan off and the other at half of its normal speed. Both fans operated at the maximum speed of 60 Hz during the normal course of the experiment.

### C. Spectrometer and detectors

Scattered electrons were detected in the SLAC 8-GeV/c spectrometer as shown in Figs. 2 and 6. The spectrometer had been dismantled for prior experiments and was reassembled and outfitted with new detectors for this experiment. Electrons from the target were focused and bent by the spectrometer magnets into a set of detectors housed in a shielded concrete hut. The spectrometer was positioned at angles of either  $\theta_0 = 21^\circ$ ,  $25^\circ$ , or  $33^\circ$  to the beam line for most of the experiment.

The detectors consisted of a subatmospheric nitrogen gas threshold Čerenkov counter, two planes of scintillator hodoscopes, ten planes of proportional wire chambers [16], and a segmented lead glass shower counter [17].

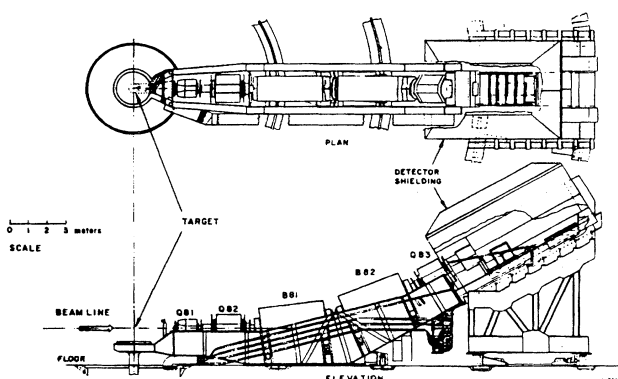


FIG. 6. The SLAC 8-GeV/c spectrometer. Particles emerged from the target and were focused by the magnets onto a set of detectors housed in a shielded concrete hut.

The detectors are shown in Fig. 7 and are discussed in more detail below. The Čerenkov counter and shower counter were used for electron identification and triggering. Together they provided a factor of  $10^4$  pion rejection while still retaining greater than 98% efficiency for detecting electrons. This reduced pion contamination of the elastic electron signal to a negligible level. Good pion rejection was also important when we measured the spectrometer acceptance using deep inelastic scattering. The wire chambers were used to measure particle trajectories. Ten planes of wire chambers were used to provide good rejection of spurious tracks and to minimize the chance of forming tracks due to accidental coincidences. Data produced by these detectors were logged onto a tape by an on-line computer system for later analysis.

### 1. Spectrometer

The SLAC 8-GeV/c spectrometer is one of three general purpose spectrometers built in the 1960s to perform electron scattering experiments in End Station A. The main features of this spectrometer have been described before [18]. It is a separated function device, in which the focusing and detection processes take place in different portions of the spectrometer. It was designed to measure momentum  $p$  (same as energy  $E'$  for electrons) and angle  $\theta$  with good acceptance for particles which scatter from extended targets along a fixed horizontal beam line. This goal was achieved through the use of vertical bending. The focusing is line to point in the horizontal plane, and point to point in the vertical plane.

The wire chambers used in this experiment covered a larger fraction of the momentum acceptance than the scintillator hodoscopes used in previous experiments and allowed the use of tracking information in analysis of the data. With this instrumentation, the expected resolution as calculated from first-order optics was roughly  $\pm 0.04\%$  in momentum and approximately  $\pm 0.04$  and  $\pm 0.9$  mrad in horizontal and vertical scattering angles  $\theta$  and  $\phi$ , respectively. The optical properties of the spectrometer are

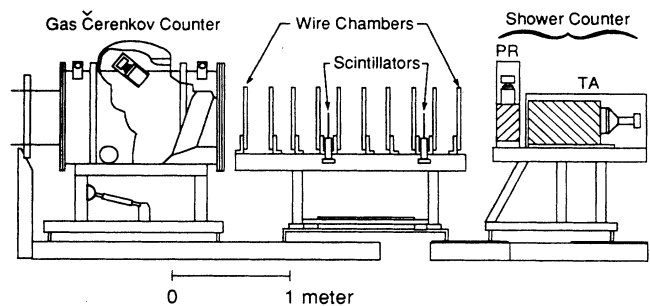


FIG. 7. Location of detectors used in this experiment. Wire chambers were used to find particle tracks. The segmented lead glass shower counter and Čerenkov counter provided particle identification and triggering. Plastic scintillators were useful in special tests. The positions of the phototubes are shown in the cutaway views of the Čerenkov counter and in the shower counter. The shaded area of the shower counter indicates the lead glass in the preradiator (PR) and total absorber (TA).

shown in Fig. 8. The original coordinates at the target were calculated from the measured trajectories of particles in the final (detector) coordinate system.

## 2. Detectors

(a) *Čerenkov counter.* After passing through the magnets of the spectrometer, particles entered a nitrogen-filled gas Čerenkov counter (CC). The counter consisted of a steel tank 2.79 m long with 0.4-mm-thick type-2024 aluminum windows at each end. The entrance window of the Čerenkov counter was separated from the 0.4-mm-thick type-6061 aluminum exit window at the last magnet by an air gap of approximately 30 cm. A segmented mirror made of slumped Lucite was used to reflect the Čerenkov light onto a single 5-in. diam Ampere XP2041 photomultiplier tube. The mirror was 6.4 mm thick and was coated with aluminum to provide reflectivity. An additional coating of magnesium fluoride was used to prevent oxidation.

The nitrogen pressure was chosen to exclude pions for most of the range of the data. Nitrogen pressure was 345

mm Hg in the first part of the experiment, during which approximately half of the data at  $Q^2=31.3$  (GeV/c)<sup>2</sup> were taken, and 500 mm Hg during the remainder of the experiment. These correspond to pion thresholds of 8.5 and 7.1 GeV/c, respectively. The data points at  $Q^2=15.7$ , 19.5, and 23.3 (GeV/c)<sup>2</sup> were taken at momenta above pion threshold in the Čerenkov counter. Cuts on shower energy and on pulse sizes for signals from the Čerenkov and preradiator counters, described later, were sufficient to remove the pion background under those kinematic conditions.

(b) *Wire chambers.* Ten planes of proportional wire chambers [16] were located just after the Čerenkov counter. Each chamber had an active area 35 cm high by 93 cm wide. The anode wires were made of gold-plated tungsten 20  $\mu\text{m}$  in diameter and were spaced at 2 mm intervals, instrumented individually in the five chambers containing horizontal wires and in pairs in the remaining chambers. The two cathode planes were made of 51- $\mu\text{m}$ -thick Mylar, coated with 8  $\mu\text{m}$  of aluminum. The anode wires were separated from these cathode planes by a gap of 4 mm in each direction. The entire assembly was held in a frame made of G10 epoxy glass board and enclosed by 76- $\mu\text{m}$ -thick Mylar gas-tight windows. The outer windows were made of a layer each of Mylar and aluminum, each 76  $\mu\text{m}$  thick, laminated together. The outer windows were spaced 1.3 cm from each of the cathode planes.

The wire chambers were operated in a proportional mode using a gas mixture (magic gas) of 65.75% argon, 30.00% isobutane [(CH<sub>3</sub>)<sub>2</sub>CHCH<sub>3</sub>], 4.00% dimethyl acetal formaldehyde [CH<sub>2</sub>(OCH<sub>3</sub>)<sub>2</sub>], and 0.25% bromotrifluoromethane (CBrF<sub>3</sub>). The gate width was 75 nsec, and each wire had a readout delay of approximately 900 nsec. For reference, the chambers were numbered sequentially in the direction that particles traversed them. In each of the even-numbered chambers, there were 176 anode wires oriented horizontally. In the odd-numbered chambers, there were 480 wires each, oriented at either +30° or -30° to the vertical plane as viewed from the front in the direction of travel of the particles. In chambers 1, 5, and 9, the wires were at +30°. In chambers 3 and 7, the wires were at -30°. The anode wires in the odd-numbered chambers were instrumented in pairs.

At the typical operating voltage of about 3.6 kV, each chamber had an average efficiency for electrons of about 98% under ideal circumstances. Ten chambers of such high efficiency were more than would be required to simply detect and measure particle tracks. Under ideal conditions, wires were fired and identified with the particle track in an average of up to 9.8 of the 10 chambers. In practice, the overall tracking efficiency was more limited by the combinatorial problem of finding tracks among multiple wire chamber hits than by individual chamber inefficiencies, as is discussed in more detail below. When the experiment was running, the chance that a wire would fire in any particular chamber due to low-energy particles produced by the beam halo or other effects was quite high, and the counting rate for each chamber as a whole was on the order of one per beam pulse. Since a

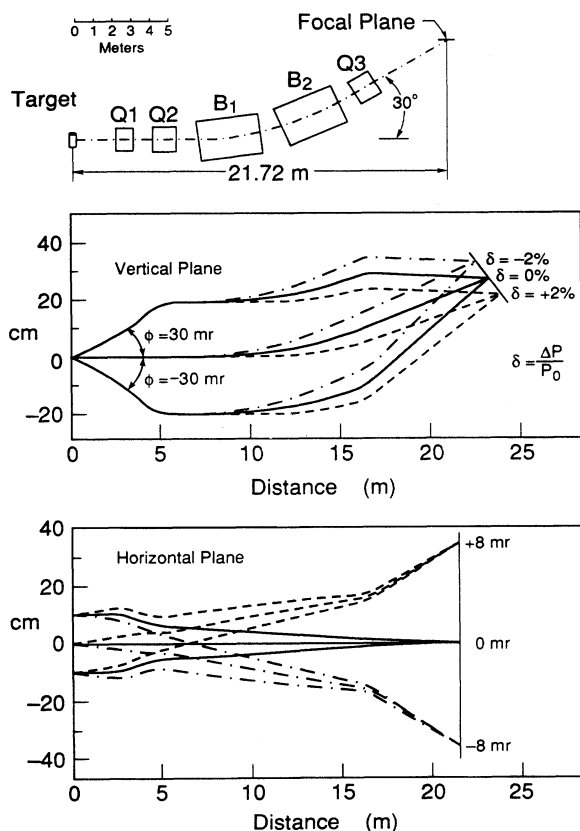


FIG. 8. Optical properties of the SLAC 8-GeV/c spectrometer. The spectrometer imaged particles with a particular horizontal angle  $\theta$  onto the same horizontal position in the final focal plane. Particles with the same fractional momentum deviation  $\delta$  from the central momentum were brought to a focus in a tilted focal plane as shown above. The production coordinates at the target were calculated from measurements of the particle trajectories in the detectors.

larger number of chambers was used than would minimally have been required to find the track, the potential background due to random coincidences was strongly suppressed.

(c) *Shower counter.* The shower counter [17] consisted of two layers of lead glass as shown in Fig. 9. The preradiator section (PR) was composed of six blocks, each 15.8 cm wide by 32 cm tall by 10.4 cm [3.2 radiation lengths (r.l.)] thick and instrumented with a single 5-in. diam Amperex XP2041 phototube. The remainder of the shower counter, called the total absorber (TA), consisted of four blocks, each 25 cm wide by 36 cm tall by 54 cm (16.8 r.l.) thick with a single 9-in. diam Amperex 60DVP phototube. The division of the detector into two layers was useful in discriminating against noise in the trigger, since electrons were very likely to cause a signal in the total absorber, preradiator, and Čerenkov counter, but pions were unlikely to create a signal in two of these detectors at the same time. (The trigger is discussed in more detail in the next section.) The signals from the phototubes were combined according to a procedure described in a later section. The energy resolution of the shower counter was roughly  $\pm 8.5\%/\sqrt{E}$  (GeV).

The magnitude of the signal from each block of the total absorber depended on the energy of the electrons which entered it. Switchable attenuators were used to keep the signal size at roughly the same value in the ADC at each of the spectrometer energy settings.

(d) *Plastic scintillators.* The detector package included two planes of plastic scintillators which covered approximately half of the acceptance. These were useful in vari-

ous tests of the performance of the other detectors and in estimating pion rates but were not used otherwise.

## D. Fast electronics and trigger

### 1. Trigger

The logic of the trigger system is shown schematically in Fig. 10. There were two levels to the trigger. The first level, called the pretrigger, consisted of coincidences between the detector signals within the beam gate, intermixed with infrequent random coincidences derived from an external pulser. The second level was called the trigger. Because of the limitations in the speed with which the computer could read the event information from the CAMAC electronics, the pretrigger was combined with a veto to limit the actual trigger rate to a maximum of 1 per 1.6- $\mu$ sec beam pulse. The total numbers of pretriggers and triggers were counted by scalers to allow for correction of the event rate for the number of pretriggers lost due to the 1-per-pulse limit. The computer was able to read and log events onto a tape in the 5.6-ms interval between beam pulses with no losses.

The goal was to create a trigger that was nearly 100% efficient for detecting electrons, while avoiding triggers that were likely to have been due to pions and muons. In the first part of the experiment, an electron candidate was defined as a coincidence between any two of the three main detectors; i.e., preradiator (PR), Čerenkov counter (CC), or total absorber (TA). Since the Čerenkov sometimes counted at several per beam pulse, this combination of detector signals produced a large number of triggers due to accidental coincidences. The TA was determined to be at least 99.8% efficient for detecting electrons using

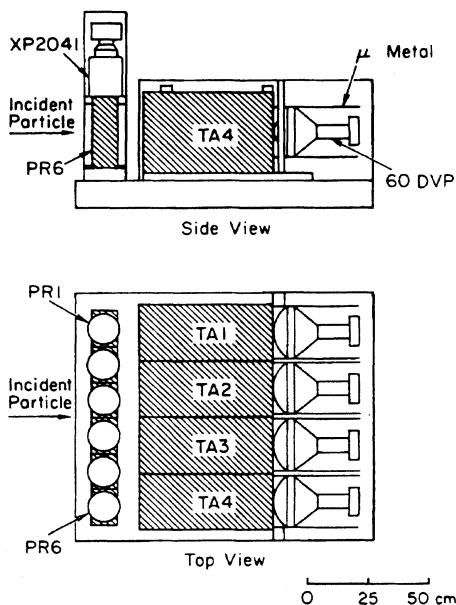


FIG. 9. Segmented lead glass shower counter used to measure electron energies and distinguish electrons from pions. (a) Side view. (b) Top view. The shaded areas indicate the glass blocks. The six PR blocks were each viewed by one XP2041 phototube from the top and the four TA blocks were each viewed by one 60DVP phototube from the back side.

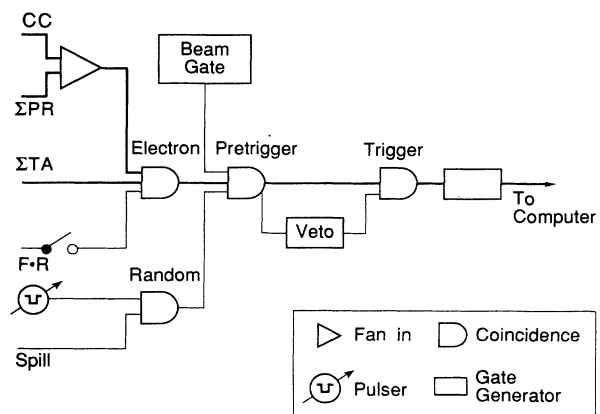


FIG. 10. Schematic representation of the trigger system logic for E136 II. The definition of an electron candidate used for the trigger in the majority of the experiment was a coincidence between either the preradiator (PR) or the Čerenkov counter (CC) and the total absorber (TA). Pretriggers composed of other combinations of the detector signals, including those from the front (F) and rear (R) planes of the plastic scintillator, were also used. The veto was initiated by the pretrigger and persisted for a time period longer than the beam pulse, effectively limiting the event rate to a maximum of one trigger per pulse.

this trigger. For the remainder of the experiment, a pre-trigger composed of a coincidence between either the PR or the CC and the TA was used. Since the TA counted at a rate that was the same order of magnitude as the electron rate, this trigger was much less subject to random coincidences. Triggers composed of other combinations of detector signals, including those from the front ( $F$ ) and rear ( $R$ ) planes of the plastic scintillator, were also useful during checkout and for special tests.

Scalers were used to count the number of potential and actual triggers for a variety of values of the trigger coincidence output width, to allow for calculation of the number of triggers lost due to electronic effects and due to the computer rate limitations mentioned above. Additional scalars, not shown in Figs. 10 and 11, counted the coincidence rates for combinations of detector signals with large arbitrary delays relative to the arrival time expected for real coincidences. This allowed the rate of accidental coincidences to be estimated.

## 2. Description of fast electronics

The signal for each detector element was split by either a linear fan out (LFO) or transformer fan out (TFO). One portion of the signal passed through a dc discriminator and then to a time-to-digital converter (TDC), latch, and

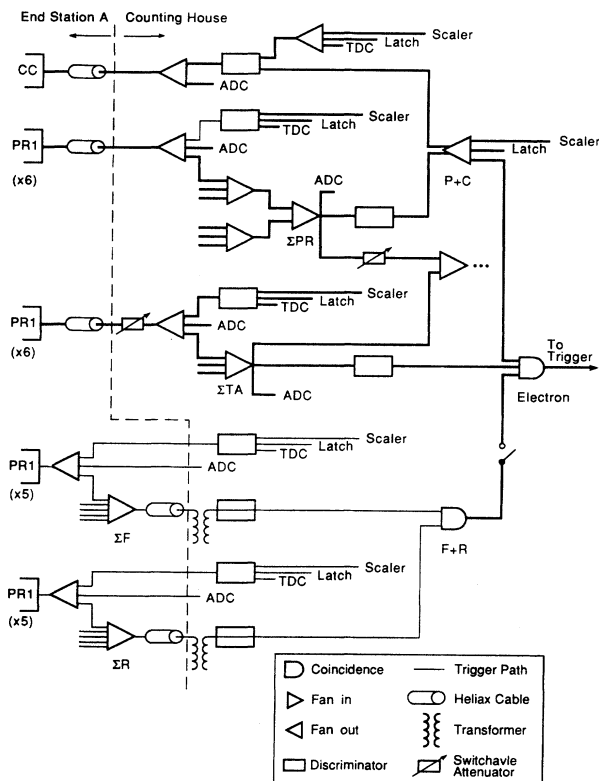


FIG. 11. Condensed electronics diagram for the second part of the experiment. The electronics for the first part were substantially similar but allowed for a trigger composed of any two of the three signals from the PR, TA, or CC. Circuitry for the counting of random coincidences is not shown.

scaler. The pulse size of the other portion of the signal was read by a charge-integrating analogue-to-digital converter. Active linear fan outs were used for the signals from the Čerenkov and shower counters to preserve the full magnitude of the input signal. Passive transformer fan outs were used for the signals from the plastic scintillators. Further details on the electronics are given in schematic form in Fig. 11.

## E. Other electronics

A dedicated PDP-11 computer read the high-speed CAMAC electronics for each event and transferred the data to a shared memory in the Vax computer. In addition, a variety of instrumentation was used to sample other signals of interest that did not change rapidly from event to event or from beam pulse to beam pulse. The toroidal charge monitors and beam steering system described earlier were connected to a dedicated LSI-11 microcomputer. The LSI-11 was in turn interfaced to the on-line Vax computer. Low-speed electronics connected by CAMAC to the Vax were used to measure and control magnet currents and wire chamber high voltages and to measure target temperatures. Data relating to the beam transport line were read via a computer link to the main accelerator control center.

The detector high voltages were checked manually once every 8-h shift. Adjustments were made when necessary to keep the voltage set to within  $\pm 0.2\%$  of the nominal value. This interval corresponded to less than  $\pm 2\%$  in photomultiplier gain, so small shifts in high voltages did not affect trigger efficiency. The wire chamber high voltages were provided by a separate supply that was continuously monitored by the computer.

## F. On-line analysis

Data acquisition and display were under the control of an on-line computer system. A sample of the data was analyzed on line to verify that the experiment was proceeding properly and to provide estimates of the cross section. This allowed decisions to be made regarding the relative allocation of running time at the various kinematic points. The data-acquisition strategy is further discussed in the next section.

## III. DATA ACQUISITION AND ANALYSIS

This section describes the kinematic range of the experiment and analysis methods used to determine the spectrometer acceptance, to test the parametrization of the spectrometer optics, and to obtain elastic cross sections from the data.

### A. Data acquisition

The primary motivation in the selection of the kinematic points for this experiment was to allow a large range of four-momentum transfer squared  $Q^2$  to be covered with the highest possible counting rate at high  $Q^2$ , within the limitations of the accelerator energy  $E$  and spectrometer momentum  $p$  and angle  $\theta_0$ . Since the accep-

tance of the spectrometer averaged over the visible length of the long target was a function of  $\theta_0$ , data were taken at only a limited number of spectrometer angles. The following subsections describe the main data categories.

### 1. Acceptance data

The kinematic conditions for the acceptance studies were chosen such that the normalized inelastic cross section  $\sigma/\sigma_{\text{Mott}}$  was smooth and nearly independent of  $E'$  and  $\theta$ . The data were then fitted to produce an acceptance function versus  $\delta \equiv \Delta E'/E'$ , the deviation of the scattered particle momentum from the central spectrometer momentum, and the scattering angular deviation  $\Delta\theta \equiv \theta - \theta_0$  of the particle relative to the angle  $\theta_0$  of the central spectrometer axis. The acceptance functions for the short and long targets were obtained at each of the spectrometer angles  $\theta_0 = 21^\circ$ ,  $25^\circ$ , and  $33^\circ$  used in the experiment. This procedure is discussed in more detail below.

### 2. Optics data

As will be demonstrated shortly, the uncertainty in acceptance for elastic data was dominated by uncertainties in the optics for reconstruction of the horizontal and vertical scattering angles  $\Delta\theta$  and  $\phi$ . The effective angular dispersions of the spectrometer were checked by placing a grid of tungsten bars [10] at the entrance aperture just before the first magnet. Electrons scattered from thin aluminum targets along the beam line, passed through holes in the grid, and were detected in the Čerenkov counter, the shower counter, and wire chambers as described earlier. These data were then analyzed to obtain the average angular spacing of the event groups which passed through the holes. The results agreed with expectations based on a physical survey of the targets and grid and implied an overall uncertainty in the acceptance of less than 2%.

### 3. Elastic data

The elastic data for this experiment were taken at forward angles to maximize counting rate, subject to the restrictions set by the maximum beam energy, maximum spectrometer momentum, and incident beam intensity. In practice the restrictions on beam energy and spectrometer momentum forced the data above  $Q^2 = 24$   $(\text{GeV}/c)^2$  to be taken at wider angles than the rest of the data set and consequently the event rate fell very quickly with increasing  $Q^2$  above this value. The cross section changed by approximately six orders of magnitude over the kinematic range of this experiment. The minimum counting rate was roughly one to two events per calendar day (approximately  $2 \times 10^{18}$  electrons on target). Because the counting rate was so low for the high- $Q^2$  elastic cross-section measurements, the condition of the apparatus was checked periodically by making measurements every 8 h or so at inelastic kinematics that produced a high counting rate.

## B. Overview of the analysis

Analysis of the raw data was performed on several Digital Equipment Corporation Vax 11/780 computers at SLAC. The goals of the analysis were to filter through the events that had been logged on to a tape and identify those with a good electron track in the detectors and to determine the efficiencies of the detectors and acceptance of the spectrometer. A multistep procedure was used, as described in detail in the following sections. The principal steps were as follows.

(1) Event selection to identify scattered electrons and reject backgrounds due to pions and spurious trigger coincidences; construction of particle tracks from wire chamber data.

(2) Reconstruction of kinematic quantities at the target using a model of the spectrometer optics.

(3) Determination of (a) the acceptance of the spectrometer averaged over the target length and (b) the effective long target length.

(4) Extraction of the elastic cross section at each kinematic point, applying corrections for detector efficiencies, radiative effects, and counting rate due to the target end caps for the short target.

The result of this process was a set of measured cross sections for elastic electron scattering from protons. Since the angular distributions of the cross sections were not measured, extraction of  $G_M^p$  and of  $F_1^p$  was performed using Eqs. (1) and (2) with the assumption that  $\mu_p G_E^p = G_M^p$ .

### 1. Event selection: Criteria used in efficiency studies

Several cuts were applied to the data to ensure that the final sample consisted of electrons scattered from the target. Data taken at elastic kinematics at low-momentum transfer, where counting rates were high and pion backgrounds were low, were useful in a number of tests to determine the efficiency of these cuts for retaining electrons. In these tests the efficiency of any particular cut was evaluated by determining the ratio of counts with and without the cut in question for a restricted data sample which passed many other cuts. The other cuts were chosen to be sufficient to determine that the particles which passed them were electrons. In general, such a restricted set of cuts would have too low an efficiency to be used in data analysis, but would assure that the resulting data sample would consist almost entirely of electrons. The restrictive cuts used in efficiency studies for this experiment were (a) a PR signal above discriminator threshold (see previous discussion on electronics), (b) a TA signal above discriminator threshold, (c) a CC signal above discriminator threshold, (d) measured shower energy  $E_s$  near the measured value  $E'$  of track energy ( $0.7 \leq E_s/E' \leq 3.0$ ), (e) a missing mass ( $0.7 \leq W^2 \leq 1.1$ ) (elastic data only), (f) target coordinates ( $-30 \text{ cm} \leq x_0 \leq 30 \text{ cm}$ ,  $-30 \text{ mrad} \leq \phi_0 \leq 30 \text{ mrad}$ ), and (g) a single good track in the wire chambers. The cut on the missing mass was only used for elastic data. Under certain circumstances, cuts on the  $F$  and  $R$  scintillator signals were also useful.

In the final analysis of the elastic cross-section data, only the cuts on the shower energy, Čerenkov discriminator, missing mass, and a less restrictive cut on track quality were used, along with an additional cut on a combination of the signals from the Čerenkov counter and the preradiator portion of the shower counter described in more detail below.

## 2. Cuts on detector signals

(a) *Energy deposited in the shower counter.* The measured shower energy  $E_s$  was defined as the sum of ADC signals, appropriately corrected for calibration, in the shower counter blocks on the track. The calculation of shower energy required the presence of a track, since only those segments of the shower counter near the track were used. The shower counter elements were divided in software into 12 vertically oriented segments and four horizontal segments. The vertical segments were chosen to be aligned with the physical divisions between the six PR blocks and four TA blocks. Tracks which pointed to the outer regions of the shower counter (within half of a segment of any edge) were rejected. Calibration constants were applied to the pulse sizes before forming this sum according to the formula

$$E_s = \sum_i (C_{PR})_{ik} (\text{PR})_i + \sum_j (C_{TA})_{jk} (\text{TA})_j$$

$$\equiv E_{PR} + E_{TA}, \quad (5)$$

where  $(\text{PR})_i$  and  $(\text{TA})_j$  represent the pedestal-subtracted pulse sizes of the shower counter elements near the track, and  $k$  was the index of the vertical segment of the shower counter nearest to the track. The calibration constants  $(C_{PR})_i$  and  $(C_{TA})_i$  had units of  $(\text{GeV})/(\text{ADC channel})$ , and were determined by minimizing the difference between the shower energy  $E_s$  and the track energy  $E'$  for a sample of the data using least-squares methods. An energy resolution for the shower counter of roughly  $\pm 8.5\%/\sqrt{E'}$  was achieved, which was adequate under the conditions of this experiment for the analysis of elastic data and for acceptance studies with inelastic data. The relatively poor resolution was caused partly by the effect of small, stray magnetic fields on the large phototubes of the TA blocks, even though they were magnetically shielded [17].

Cuts were applied to limit the ratio of shower energy to track energy to the range  $0.7 \leq E_s/E' \leq 3.0$ . The central value for single electrons is 1; the high upper limit accepts multiple electrons. Typical shower energy spectra are shown in Fig. 12 for data at elastic and inelastic kinematics. Scatter plots of PR and TA pulse signals normalized to  $E'$  are shown in Fig. 13.

(b) *Čerenkov counter.* The Čerenkov counter was required to have fired with a pulse height sufficient to trigger a hardware discriminator. Under the conditions of this experiment, the threshold of this discriminator was sufficiently low to provide a high efficiency for detecting electrons. The efficiency of the cut was determined to be 98.9% for the first part of the experiment (nitrogen pressure of 345 mm Hg) and 99.5% for the second

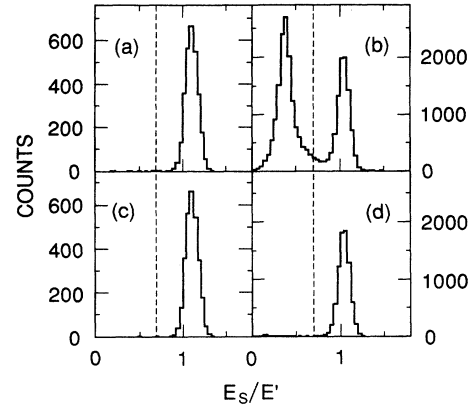


FIG. 12. Typical shower energy spectra for data taken at (a) elastic kinematics under conditions that would yield a small pion rate; (b) inelastic kinematics under conditions yielding a large number of pions. The abscissa is the ratio of shower energy  $E_s$  to track energy  $E'$ . Electrons would be expected to populate the portion of this plot near  $E_s/E' = 1.0$ . The dashed line shows the lower cut on shower energy. (c) The same spectrum as in (a), with additional cuts on the Čerenkov discriminator and  $P_{CP}$ , a combination of Čerenkov and PR pulse heights as described in the text. (d) The same spectrum as in (b), with additional cuts on the Čerenkov discriminator and  $P_{CP}$ .

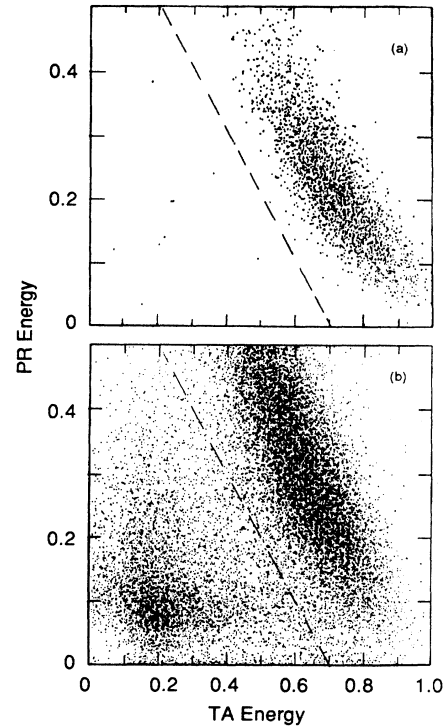


FIG. 13. Scatter plots of PR and TA pulse signals normalized to  $E'$  with no cut on the CC pulse height. The lower bound on  $0.7 \leq E_s/E' \leq 3.0$  rejects particles to the left of the dashed line. (a) Elastic data; (b) inelastic data.

part (nitrogen pressure of 500 mm Hg) by using elastic scattering data at low-momentum transfer according to the method described above.

(c) *Čerenkov and PR combination.* There was a high probability that electrons would both deposit a large amount of energy in the preradiator layer of the shower counter and yield a large pulse size in the Čerenkov counter. There was a low probability for the signals from electrons in both of these counters to be small. To make use of this, the quantity  $P_{CP} \equiv P_{CC} + P_{PR}$  was defined, where  $P_{PR} \equiv E_{PR}/E'$  was the normalized pulse size deposited in the preradiator as defined above and  $P_{CC}$  was defined as the Čerenkov pulse area scaled by a factor chosen to match its distribution roughly with that of the preradiator.

The primary mechanism for a pion to create Čerenkov light was through the production of knock-on electrons. Knock-on electrons would tend to produce a small pulse size in the Čerenkov counter because in general they would not be oriented in the direction of travel of the pion and would carry typically only a few tens of MeV of energy. Knock-on electrons produced in or before the Čerenkov counter would tend not to fire the PR or TA, but the pion which produced them could interact hadronically in the shower counter and so cause a trigger. A pion interacting in the shower counter would in general yield a smaller signal than that from an electromagnetic shower.

The cut on the CC-PR combination was defined such that events with  $0.2 \leq P_{CP} \leq 0.85$  were accepted. The motivation for this cut was to exclude pions while still retaining a large efficiency for detecting electrons. In a study of events in elastic scattering which populated the kinematically forbidden region of missing mass below the elastic peak, it was found that an abnormally large number of such events populated the region  $P_{CP} \leq 0.2$  or  $P_{CP} \geq 0.85$ . On closer inspection, events with large  $P_{CP}$  and a low missing mass often were found to have fired a large number of closely spaced wires in the wire chambers, so were probably due to particles which interacted in the chambers or other intervening material before reaching the shower counter. Events with low  $P_{CP}$  were also found to represent an unusually large portion of the kinematically forbidden data set, and were probably due to pions which showered in the TA in coincidence with a knock-on or random hit in CC.

The efficiency of the  $P_{CP}$  cut was evaluated using elastic scattering data at low-momentum transfer, and it varied from approximately 98% to 99%, depending on the particle energy  $E'$  due to the effect of the changing shape of the preradiator energy spectrum. The uncertainty in efficiency at any particular value of  $E'$  was less than  $\pm 0.5\%$ .

### 3. Total pion rejection factor

Under the conditions of this experiment, the greatest source of background from particles other than electrons was due to strongly interacting particles, such as pions, which generated enough light in the total absorber to cause a trigger. Muons were much less likely to cause a

trigger since they did not produce large pulses in the shower counter. The total pion rejection factor was determined by studying inelastic data under conditions that yielded a nearly pure pion data sample.

The pion rate was estimated from the coincidences between the  $F$  and  $R$  scintillator counters by subtracting the accidental coincidence rate, and scaling the result by a factor of 2 to account for the mismatch in size between the scintillators and other detectors. The pion rate estimated in this manner agreed with that predicted from a fit to previous pion production data to within about  $\pm 30\%$  where such data existed. The combination of cuts on shower energy, Čerenkov discriminator, and  $P_{CP}$  produced a typical pion rejection factor of roughly  $10^4:1$ . The total inefficiency of the cuts that produced this rejection factor was typically less than 2%. With this rejection, contamination of the elastic electron signal was reduced to a negligible level.

### 4. Good track

The wire chamber data were analyzed for the presence of identifiable tracks in a series of steps. First, groups of adjacent wires that fired within each chamber were located, and the centroids with an appropriate uncertainty were used in track finding. Hypothetical tracks were then formed by finding straight lines between all possible pairs of group centroids in the five chambers with horizontal wires. A track was retained if hit wires consistent with that track were found in at least three other chambers, of which at least two had to be from chambers with diagonal wires. A chamber was considered to have fired for a hypothetical track if the track passed within a  $\pm 3$  wire spacing of a group centroid in that chamber. The tracks were further required to be clearly identifiable according to the following criteria.

(a) Only those tracks were retained which pointed to regions of the shower counter in which significant energy was deposited.

(b) Multiple track events were retained and treated as multiple good events if the Čerenkov counter pulse size and the amount of energy deposited in the shower counter for an event, as described above, were consistent with the observed number of tracks.

(c) There would be no more than a total of 30 hit wires or groups of wires in any event to minimize the possibility of finding tracks that would reconstruct to incorrect values of missing mass outside the acceptance.

(d) There could be no more than 20 hit wires or groups of wires in any one of the ten chambers.

Events were required to have either exactly one clear track according to the above criteria or  $N$  tracks consistent with the amount of shower energy and Čerenkov pulse size expected for  $N$  electrons. Typical tracks are shown in Fig. 14.

The average number of wires per group for the elastic data in this experiment was typically 1.1; the average number of groups per chamber was approximately 1.3 for events with good tracks. Under these conditions, the track-finding program proved very reliable. Tracks for elastic data were matched with hit wires in an average of

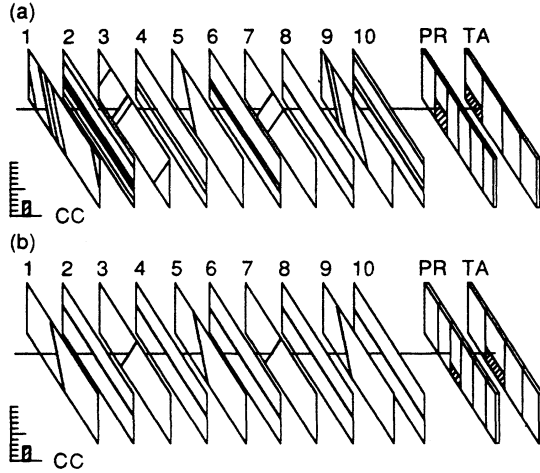


FIG. 14. Typical tracks formed from data in the proportional wire chambers. The pulse height of signals from the Čerenkov and shower counter phototubes are indicated by the height of the shaded area of each element. (a) Track found in an event for which a large number of spurious wires had fired. Such events were common during measurements at inelastic kinematics, especially when the beam was slightly misdirected or a significant beam halo was present. The presence of ten chambers for track measurement provided sufficient redundancy to retain high efficiency (typically greater than 96%) for finding the track, even under such conditions. (b) A much more typical track for events taken at elastic kinematics. The absence of spurious wire hits allowed the tracking efficiency to exceed 99% for the majority of this experiment.

typically 9.7 chambers. The efficiency for finding good tracks was generally between 98% and 99.5% for elastic data. Wire chamber performance was slightly worse for data in the inelastic region, and depended in part on event rate and on beam tuning due to the presence of a larger number of spurious wire hits. Tracking efficiency was degraded during such conditions but was never worse than 93%.

Further details on the construction and performance of the wire chambers and tracking routine, including a discussion of the effects of different choices of gas mixtures, the placement of the support wires, and details of the electronic readout system, are contained in Ref. [16].

### C. Acceptance

#### 1. Definition of coordinates

In the analysis, it was convenient to consider the initial trajectories of the scattered particles in three different coordinate systems. The laboratory kinematics of the scattering reaction are described in a polar coordinate system (coordinates denoted without subscripts) defined with the  $z$  axis along the incident beam direction, where  $\theta$  is the polar scattering angle and  $\phi$  is the azimuthal angle. The direction  $\phi=0$  is in the horizontal plane. Particles are detected in the spectrometer acceptance centered around the optical axis located at  $\phi_0=0$  and a central scattering angle  $\theta_0$ .

The coordinate system used to describe particle trajectories inside the spectrometer (denoted with the subscript  $s$ ) follows the TRANSPORT computer program convention [19]. The origin is at the point of intersection of the beam line and the spectrometer axis with the  $z$  axis directed along the optical axis. In this coordinate system, particles incident on the spectrometer are described by  $x_s$  and  $y_s$ , the horizontal and vertical displacements of the scattering point from the origin, and  $\theta_s$  and  $\phi_s$ , the horizontal and vertical angular projections. The momentum deviation is  $\delta=\Delta p/p$ .

The trajectories of the particles in the final coordinate system, after passage through the spectrometer into the region occupied by the detectors, are expressed in terms of variables in a right-handed coordinate system that are denoted by the subscript  $f$ . This final coordinate system has its origin at the spectrometer momentum focal plane, with the  $z$  axis oriented along the optical axis. In this system,  $x_f$  and  $y_f$  are the horizontal and vertical displacements and  $\theta_f$  and  $\phi_f$  are the horizontal and vertical angles.

The usual five parameters needed to describe a charged-particle trajectory in a magnetic system  $(x_s, \theta_s, y_s, \phi_s, \delta)$  can be reduced to four by using the constraint that particles in this spectrometer originate near  $y_s=0$ , because the vertical size of the beam spot is small (on the order of a few millimeters). With this constraint, measurements of four parameters for each track in the detectors  $(x_f, \theta_f, y_f, \phi_f)$  can be used to reconstruct four parameters  $(x_s, \theta_s, \phi_s, \delta)$  of the scattered particles at the target.

The relation between the spectrometer coordinates  $\theta_s$  and  $\phi_s$  and the physical polar coordinates  $\theta$  and  $\phi$  which determine the kinematics of the scattering reaction is

$$\begin{aligned} \tan(\phi) &= \tan(\phi_s) / \sin(\theta_0 + \theta_s), \\ \cos(\theta) &= \cos(\theta_0 + \theta_s) \cos(\phi). \end{aligned} \quad (6)$$

The solid angle subtended in a range  $(\Delta\theta, \Delta\phi)$  centered at  $\theta=\theta_0$  and  $\phi=0$  is  $\Delta\Omega = \Delta\theta\Delta\phi \sin\theta_0$ . Inspection of Eq. (6) shows that the main difference between the azimuthal angle  $\phi$  and the spectrometer angle  $\phi_s$  for small  $\theta_s$  is a factor of approximately  $\sin\theta_0$ ; i.e.,  $\phi \sin\theta_0 \approx \phi_s$ . The data were binned versus  $\phi \sin\theta_0$  to minimize the variation of the acceptance function with spectrometer angle. The maximum range in  $\phi \sin\theta_0$  is approximately the same for all values of  $\theta_0$  used.

#### 2. Spectrometer optical properties

The optical properties of the spectrometer required to reconstruct particle trajectories at the target can be summarized as a coordinate transformation expressed as a truncated Taylor series in the form

$$Q_k = \sum_{i=1}^4 \langle Q_k | q_i \rangle q_i + \sum_{i=1}^4 \sum_{j=1}^i \langle Q_k | q_i q_j \rangle q_i q_j, \quad (7)$$

where  $q_i = \{x_f, \theta_f, y_f, \phi_f\}$  and  $Q_k = \{x_s, \theta_s, \phi_s, \delta\}$ . The optics coefficients  $\langle Q_k | q_i \rangle$  and  $\langle Q_k | q_i q_j \rangle$  can be predicted from the magnet properties, or they can be obtained from measurements. Good knowledge of the spectrome-

ter optics coefficients was required for this experiment because the acceptance was determined by software cuts on the reconstructed particle momenta and angles. We therefore made extensive particle studies of the optics as part of this experiment. These studies were comprised of two parts: (a) a careful reexamination of the previous optics data [18] obtained shortly after the spectrometer was built in 1967, and (b) a new measurement of a subset of the optics coefficients using a set of thin targets and a grid mask in front of the spectrometer [10,20]. The main goal of this work was to understand the uncertainty in the acceptance arising from uncertainty in the optics coefficients. Another purpose for the grid mask measurements was to verify that the spectrometer was performing in 1983 and 1984 the same as it had been in 1967, since it had been partially disassembled for another experiment and then reassembled just before E136.

(a) *1967 optics data.* Data were taken in 1967 using the direct beam to measure the optical properties of the spectrometer. For these tests, the spectrometer was placed directly in the path of the beam, and three small bending magnets were installed just in front of the spectrometer to control the beam path. The detectors were removed from the spectrometer, and incident and final beam trajectories were measured by observing beam spots on zinc sulfide screens. Measurements were taken at beam energies of 3, 6, 8, and 9 GeV. Further details of the apparatus and results are contained in Kirk *et al.* [2].

Spectrometer optics coefficients were determined in 1968 by fits to the data at each energy and to the combined data set. We refit the old data to verify the coefficients. We then studied the effect on the acceptance phase volume from using coefficients derived from fits to data taken at different spectrometer momenta. With the exception of the data at 9 GeV, where the spectrometer properties may be different than at lower momenta due to the onset of saturation in the magnet iron, the differences between the results using different coefficients are less than 1%.

(b) *Grid mask studies.* In this experiment some special measurements were made using a grid mask at the entrance of the spectrometer to check a subset of the major coefficients required for reconstructing  $\theta_s$  and  $\phi_s$ . For these measurements a set of thin Al targets at several locations along the beam line were used (see Fig. 3). By adjusting the movable slits at the entrance to the spectrometer set at a scattering angle of  $\theta_0 = 15.5^\circ$ , it was possible to restrict the acceptance to include electrons scattered from individual Al targets corresponding to fixed locations in  $x_s$ . Data were then taken at kinematic settings in the deep inelastic region that generated smooth, slowly varying distributions of electrons across the acceptance. The experimental arrangement is sketched in Fig. 15.

The location of the holes in the grid with respect to the location of the beam, target, and spectrometer axis was determined carefully by direct surveying. After suitable corrections for the incident spectral shapes (as measured with the grid removed), it was possible to compare the images of the holes in the grid mask (as measured by reconstructing particle trajectories) with values expected from the direct survey. Fits were made to minimize the

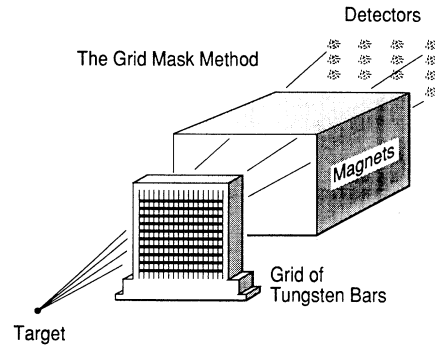


FIG. 15. Schematic representation of the grid mask method. A grid of tungsten bars is placed between a point target and the magnets of the spectrometer, forming a pattern of events in the detectors.

difference between the centers of the holes imaged by the particles and those determined by surveying, to obtain a subset of the optics coefficients. In these fits the coefficients not directly measured in the grid mask technique, in particular those depending on  $\delta$ , were fixed at the nominal values. Measurements were made at several values of  $x_s$  for a 6.5-GeV/c spectrometer momentum setting, and at  $x_s = 0$  for 4.5- and 8.5-GeV/c momentum settings.

Studies were then made comparing the acceptance phase-space volume, using coefficients determined in part from the grid mask data, with those determined from the 3-GeV/c 1967 optics data. Details are given in Ref. [20]. These studies showed that the acceptance obtained using various coefficients derived from the new data varied by as much as 3% from that given by the 3-GeV/c 1967 coefficients, with combined statistical and systematic uncertainties on the order of 2%. These differences were comparable to the differences among the 1967 results.

A main conclusion of this work is that the reassembled spectrometer behaved, within the errors of our test, as it did in 1967, and therefore we can use the 1967 optics coefficients to analyze the data from this experiment. As a result of this work, we assign an overall uncertainty of  $\pm 2\%$  on the cross sections due to uncertainty in the acceptance arising from lack of knowledge of the reconstruction coefficients. The coefficients determined from the 1968 fit to the 3-GeV/c 1967 data, given in Table III, were used to analyze all the data reported in this paper. Subsequent higher-precision studies of the acceptance done as part of a successive set of End Station A experiments [21,22] gave optics results that were 2% lower in angular acceptance than those obtained with our choice of coefficients. The cross sections reported here have thus been increased by 2% to include the effect of these acceptance corrections.

### 3. Overview of acceptance concepts

The acceptance of the spectrometer was not uniquely determined by any one set of fixed apertures or slits, but was defined by a combination of internal apertures and by

TABLE III. Reverse optics coefficients used to analyze data from this experiment. These coefficients come from a least-squares fit done in 1968 to the 3-GeV subset of direct beam data taken in 1967.

	$x_0$ (cm)	$\theta_0$ (mrad)	$\phi_0$ (mrad)	$\delta_0$ (%)
$x_f$ (cm)	4.5324±0.0479	0.1849±0.0029	-0.0410±0.0095	0.0017±0.0011
$\theta_f$ (mrad)	-4.2736±0.0447	0.0347±0.0027	0.0442±0.0089	-0.0009±0.0010
$y_f$ (cm)	0.0527±0.0173	0.0079±0.0010	-0.0242±0.0034	-0.3385±0.0004
$\phi_f$ (mrad)	-0.0141±0.0057	-0.0030±0.0003	-0.9301±0.0011	-0.0001±0.0001
$x_f x_f$	0.0387±0.0298	0.0040±0.0018	-0.0014±0.0059	-0.0028±0.0007
$x_f \theta_f$	-0.0713±0.0561	-0.0075±0.0034	0.0023±0.0111	0.0053±0.0012
$x_f y_f$	0.0145±0.0106	0.0146±0.0006	-0.0020±0.0042	0.0007±0.0000
$x_f \phi_f$	-0.0066±0.0037	-0.0005±0.0002	-0.0000±0.0007	-0.0000±0.0000
$\theta_f \theta_f$	0.0334±0.0264	0.0036±0.0016	-0.0010±0.0052	-0.0025±0.0006
$\theta_f y_f$	-0.0083±0.0099	-0.0141±0.0006	0.0029±0.0020	-0.0007±0.0002
$\theta_f \phi_f$	0.0058±0.0035	0.0004±0.0002	0.0000±0.0007	0.0000±0.0000
$y_f y_f$	0.0067±0.0042	0.0002±0.0002	-0.0040±0.0008	-0.0007±0.0000
$y_f \phi_f$	0.0002±0.0014	-0.0000±0.0000	-0.0011±0.0003	0.0013±0.0000
$\phi_f \phi_f$	0.0006±0.0004	0.0000±0.0000	0.0002±0.0000	0.0000±0.0000

the sizes of the detectors. For a thin target, the acceptance was independent of the spectrometer central angle  $\theta_0$ , and depended only on the particle coordinates  $\theta_s$  and  $\phi_s$  and momentum  $\delta = \Delta p / p$ . The acceptance also varies with  $x_s$ , the horizontal position of the incident trajectory relative to the spectrometer axis. Consequently, for extended targets of length  $L$  along the beam, in which particles originate from the projected length  $x_s = \pm L / 2 \sin \theta_0$ , the acceptance averaged over the target length depends upon the spectrometer setting  $\theta_0$ . Since the elastic cross section is a function only of scattered energy and polar angle  $\theta$  and does not depend on  $\phi$ , we want to bin the data versus physical coordinates  $\theta$  and  $\delta$  summed over  $\phi$ . To calculate cross sections, we need the  $\phi$  acceptance averaged over the target length for each bin ( $\Delta\delta, \Delta\theta$ ).

A total acceptance volume  $\Delta\Omega_{\text{tot}} = \Delta\theta_{\text{tot}} \Delta\phi_{\text{tot}} \sin\theta_0$  inside the spectrometer aperture was the region over which elastic counts are summed and cross sections calculated. The limits of  $\Delta\Omega_{\text{tot}}$  were set by software cuts on the values of reconstructed particle trajectories. For each bin ( $\Delta\delta, \Delta\theta$ ) centered at  $(\delta, \theta)$ , the  $\phi$  acceptance was

$$\Delta\phi = A(\delta, \theta) \Delta\phi_{\text{tot}}, \quad (8)$$

where  $A(\delta, \theta) \leq 1$  is an acceptance function determined empirically as described below. The function  $A(\delta, \theta)$  represents the fraction of  $\Delta\phi_{\text{tot}}$  averaged over the target length that is effective at a particular  $(\delta, \theta)$  due to spectrometer apertures and sizes of the detectors.

The 65-cm target was too long to be completely visible in any portion of the spectrometer at any of the values of spectrometer angle  $\theta_0$  used in this experiment. Furthermore, because of restrictions presented by the shields and

spectrometer apertures, the visible length of the long target was different for each value of  $\theta_0$  (see Fig. 4). The length of the short target (25 cm) was chosen so that its projected length as seen by the spectrometer was small. The criterion for this choice was that the acceptance averaged over the target length did not vary with spectrometer angle  $\theta_0$  by more than 0.5%, as would be the case for a pointlike target. The fraction of the long target visible at each of the spectrometer angle settings was determined by comparing the counting rate for inelastic scattering in a central region of the spectrometer from the long and short targets. The determination of the target length acceptance is discussed in more detail below.

#### 4. Determination of the acceptance function

At each of the spectrometer angle settings, the acceptance of the apparatus averaged over the length of each target was studied using deep inelastic electron scattering in kinematic regions where the cross section is well known. A central “fiducial” region in  $(\delta, \theta, \phi)$  space was defined in software such that for the short target, all particles with reconstructed coordinates within this region passed inside all of the apertures of the spectrometer. The boundaries of the fiducial region were  $\Delta\theta = \pm 5$  mrad,  $\Delta\phi \sin\theta_0 = \pm 15$  mrad, and  $-2.5\% \leq \delta \leq 1.5\%$ . They were determined by examination of the results of a Monte Carlo model of the spectrometer, target, and detectors to locate a region of clear aperture for a 25-cm-long target at  $\theta_0 = 21^\circ - 33^\circ$ .

The average number of counts per  $(\delta, \theta)$  bin in the fiducial region was defined as

$$N_{\text{fid}} \equiv \frac{\sigma'_{\text{inel}}(\delta=0, \theta=\theta_0)}{M_{\text{fid}}} \frac{\sum_{\delta=-2.5\%}^{1.5\%} \sum_{\theta=-5 \text{ mrad}}^{5 \text{ mrad}} \sum_{\phi \sin\theta_0=-15 \text{ mrad}}^{15 \text{ mrad}} N(\delta, \theta, \phi)}{\sigma'_{\text{inel}}(\delta, \theta)}, \quad (9)$$

where  $N(\delta, \theta, \phi)$  was the number of counts in each bin,  $M_{\text{fid}}$  was the total number of  $(\delta, \theta)$  bins in the fiducial region, and  $\sigma'_{\text{inel}}$  represents a model for the inelastic cross section [23], including radiative corrections [24], used to

correct the acceptance data for known variations of the cross section with scattered energy and angle. The quantity  $N_{\text{fid}}$  represents the number of counts per  $(\delta, \theta)$  bin one would obtain if the cross section were independent of

scattered energy and angle. The kinematic conditions for the acceptance studies were chosen to minimize dependence on the model for  $\sigma'_{\text{inel}}$  by selecting regions such that the normalized inelastic cross section  $\sigma'/\sigma_{\text{Mott}}$  was smooth and nearly independent of  $\delta$  and  $\theta$ .

For the short target  $N(\delta, \theta, \phi)$  was corrected for the counting rate due to target end caps before forming the sum in Eq. (9), using data taken with the short empty target according to the formula

$$N(\delta, \theta, \phi)|_{\text{corr}} = N(\delta, \theta, \phi)|_{\text{full}} - \frac{(tQ/C_R)_{\text{full}}}{(tQ/C_R)_{\text{empty}}} N(\delta, \theta, \phi)|_{\text{empty}}. \quad (10)$$

Here  $t$  represents the total amount of target material (expressed in  $\text{g}/\text{cm}^2$ ) of the end caps for either the full or empty target, and  $Q$  is the amount of beam charge. Notice that the end caps of the empty targets were thicker than those of the hydrogen targets. The radiative correction factors  $C_R$  in Eq. (10) were calculated for the end caps of each target taking into account the differences in physical construction. The end cap correction for inelastic data with the short target was typically about 8%. The inelastic radiative corrections generally matched for the full and empty target end caps to within  $\pm 1\%$ .

The variation of the  $\phi$  acceptance with  $\delta$  and  $\theta$  outside the fiducial region was determined for each target by comparing the counting rate at each  $(\delta, \theta)$  bin to the fiducial value in the following manner. The quantity

$$A(\delta, \theta) = \frac{\Delta\phi_{\text{fid}}}{\Delta\phi_{\text{tot}}} \frac{\sigma'_{\text{inel}}(\delta=0, \theta=\theta_0)}{N_{\text{fid}} \sigma'(\delta, \theta)} \times \sum_{\phi \sin\theta_0 = -30 \text{ mrad}}^{30 \text{ mrad}} N(\delta, \theta, \phi) \quad (11)$$

represents the ratio of the counting rate at any  $(\delta, \theta)$  bin summed over  $\Delta\phi_{\text{tot}}$  to the counting rate in the fiducial region, corrected for the intrinsic variation in cross-section and radiative corrections, and for the increased range in azimuthal scattering angle  $\Delta\phi_{\text{tot}}$  over that of the fiducial region  $\Delta\phi_{\text{fid}}$ . These data were fitted to produce an acceptance function of the form

$$A(\delta, \theta) = \sum_{m=0}^7 \sum_{n=0}^7 c(m, n) \delta^m \theta^n. \quad (12)$$

With the normalization given above,  $A(\delta, \theta)$  may be interpreted as the effective  $\phi$  acceptance averaged over the target length at a particular value of  $\delta$  and polar angle  $\theta$  for an electron to pass inside all of the apertures of the spectrometer and be detected. An example of such an acceptance function is shown in Fig. 16. The acceptance function  $A(\delta, \theta)$  was determined separately for the long and short hydrogen targets at each spectrometer angle  $\theta_0$ .

The data were summed over the  $\Delta\phi_{\text{tot}}$  range  $-30 \text{ mrad} \leq \phi \sin\theta_0 \leq 30 \text{ mrad}$ . The range of  $\theta$  and  $\delta$  was determined from each set of acceptance data such that

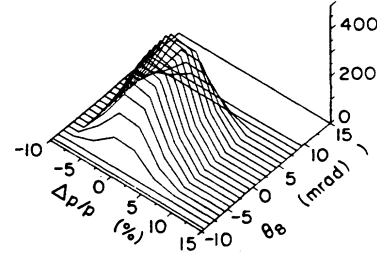


FIG. 16. Example of an acceptance function for the SLAC 8-GeV/c spectrometer and detectors as discussed in the text. The function may be interpreted as the effective  $\phi$  acceptance for an electron to pass inside all of the apertures of the spectrometer and be detected, averaged over the target length as a function of  $\delta$  and  $\Delta\theta$ .

the acceptance function at the edges was not less than a factor of 3 lower than the central value. Nominal limits were  $\Delta\theta_{\text{tot}} = \pm 6 \text{ mrad}$  and  $\delta = (-5.0 - +4.5)\%$ . The data were binned such that before application of these cuts, the events populated roughly 18 bins of 1 mrad each in  $\theta$  and 25 bins of 0.5% each in  $\delta$ . For each set of acceptance data, there were about 100 000 total counts, yielding an average of several hundred counts per bin. The values of  $\chi^2$  for the acceptance fits were typically 1.0–1.4 per degree of freedom.

The elastic data populated only a small portion of the acceptance. An example of an elastic peak viewed in the  $(\delta, \theta)$  plane is shown in Fig. 17. The acceptance boundary in the  $\theta$  direction limited coverage of the elastic peak under the kinematic conditions of this experiment. Uncertainties in the optical transformation that gives the  $\theta$  coordinates of the particles directly influenced the final uncertainty on the cross section. The same was true for the  $\phi$  coordinate, since definite cuts were applied in  $\phi$  to calculate the cross section. The primary effect of uncertainties in the transformation for  $\delta$ , however, was on the resolution with which the missing mass peak was observed. Since the acceptance boundary in  $\delta$  was not a

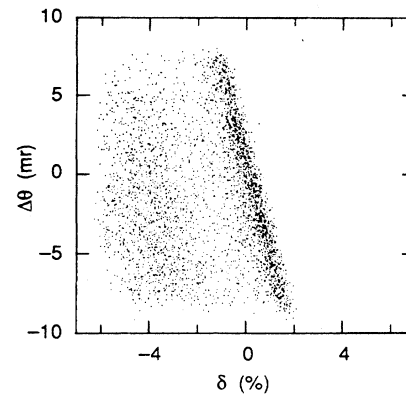


FIG. 17. Example of an elastic peak as viewed in the  $(\delta, \theta)$  plane. The acceptance boundary in the  $\theta$  direction limited coverage of the elastic peak for the kinematics of this experiment. The peak appears as a band near  $\delta=0$ , and the radiative tail from QED effects is evident on the negative  $\delta$  side of the peak.

TABLE IV. Check of the relative acceptance normalization between long and short targets, using elastic cross-section data taken at identical kinematics. Columns three and four give the cross sections for data from the long and short targets, using the corresponding acceptance functions and corrections as explained in the text. The last column gives the difference divided by the average of these measurements. The errors are dominated by statistical uncertainty and do not include those systematic effects which cancel in the ratio.

$E_0$ (GeV)	$\theta_0$ (deg)	$(d\sigma/d\Omega)_L$ (nb/sr)	$(d\sigma/d\Omega)_S$ (nb/sr)	$\frac{\Delta(d\sigma/d\Omega)}{\langle d\sigma/d\Omega \rangle}$ (%)
7.597	21.01	$(6.98 \pm 0.08) \times 10^{-2}$	$(7.12 \pm 0.06) \times 10^{-2}$	$-2.0 \pm 1.4$
13.21	21.01	$(8.06 \pm 0.31) \times 10^{-4}$	$(8.07 \pm 0.30) \times 10^{-4}$	$-0.1 \pm 5.4$
5.499	33.01	$(2.02 \pm 0.04) \times 10^{-2}$	$(2.05 \pm 0.04) \times 10^{-2}$	$-1.5 \pm 3.0$
Average:				$-1.9 \pm 1.4$

limiting factor in the coverage of the missing mass peak, uncertainties in the calculation of  $\delta$  were more tolerable.

For convenience, the elastic data were binned as two-dimensional histograms in  $W^2$  and  $\theta$ . The acceptance function was applied to the data by calculating the value of  $\delta$  that corresponded to the central value of each  $(W^2, \theta)$  bin.

#### 5. Normalization between short and long targets

The normalization between long and short visible target lengths was determined at each spectrometer angle by comparing corrected short and long target counting rates in the fiducial region. Small corrections were also applied to account for differences in dead time and counting efficiency between the short and long target data. The resulting normalization factor was defined as

$$F = \frac{[N_{\text{fid}} / (Q\sigma'_{\text{inel}}\rho LD)]_{\text{long}}}{[N_{\text{fid}} / (Q\sigma'_{\text{inel}}\rho LD)]_{\text{short}}}, \quad (13)$$

where for each target  $N_{\text{fid}}$  was the counts in the fiducial region as defined above,  $Q$  was the beam charge,  $\sigma'_{\text{inel}}$  was the radiatively corrected inelastic cross section at the center of the spectrometer,  $\rho$  was the target density,  $L$  was the length, and  $D$  was the total hardware correction due to electronic and trigger dead time and detector inefficiencies. The factor  $F$  can be interpreted as a measure of the fraction of the long target length visible between the shields at a given scattering angle  $\theta_0$ .

To check the relative acceptance normalization, elastic data were taken at  $Q^2=5$  and  $12$   $(\text{GeV}/c)^2$  with both targets under identical kinematic conditions. The average of the ratios of elastic cross-section results, determined by procedures described in the next section, agreed to within  $(-1.9 \pm 1.4)\%$ . Data used to obtain this value are summarized in Table IV. Uncertainties affecting the final cross sections are discussed in more detail below.

#### D. Radiative corrections

Elastic radiative corrections were applied to the data using the formula of Mo and Tsai [25] improved to include modifications to the internal bremsstrahlung due to the energy dependence of the cross section, the Landau ionization tail, and  $\mu$ ,  $\tau$ , and quark vacuum polarization terms [22]. The radiative correction factor was typically

1.45. To check the dependence of these corrections on external radiators, elastic data were taken with the short target at  $Q^2=5$   $(\text{GeV}/c)^2$ , both with and without an additional 2.3% radiator upstream of the target. The final corrected cross sections agreed to within  $(2.0 \pm 1.5)\%$  (see Table IX). As a check on possible angle dependence of radiative corrections and other effects, measurements were also made at  $Q^2=5$   $(\text{GeV}/c)^2$  with the long target at each of the three scattering angles ( $21^\circ$ ,  $25^\circ$ , and  $33^\circ$ ) used in the experiment. The results for  $Q^4 G_M^p$  agreed to within  $(1.0 \pm 1.0)\%$ , implying an agreement in cross sections to within  $(2.0 \pm 2.0)\%$ .

Figure 18 shows the dependence of the radiatively

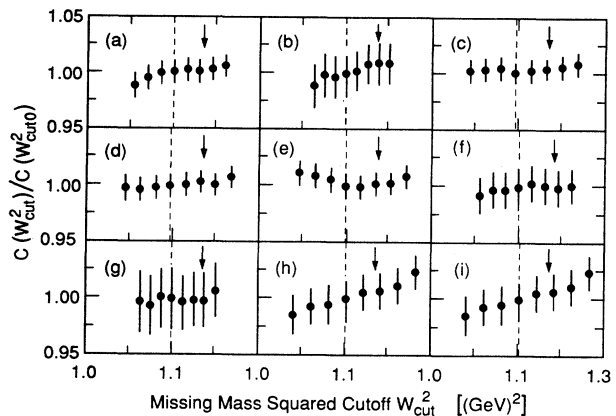


FIG. 18. Dependence of elastic cross sections on the  $W^2$  cutoff for radiative corrections. The ratio of  $C(W_{\text{cut}}^2)/C(W_{\text{cut0}}^2)$  is plotted vs the missing mass squared cutoff, where  $C(W_{\text{cut}}^2)$  represents the radiatively corrected number of counts summed vs  $W^2$  over the elastic peak and radiative tail up to the given value of  $W_{\text{cut}}^2$ , and  $W_{\text{cut0}}^2$  is the nominal cutoff [typically 1.10  $(\text{GeV}/c)^2$ ]. The nominal cutoff  $W_{\text{cut0}}^2$   $(\text{GeV})^2$  chosen for each measurement is shown as a dashed line. An arrow indicates the kinematic threshold for pion production. (a)  $Q^2=2.9$   $(\text{GeV}/c)^2$ ,  $\theta=21^\circ$ , long target; (b)  $Q^2=3.6$   $(\text{GeV}/c)^2$ ,  $\theta=25^\circ$ , long target; (c)  $Q^2=5.0$   $(\text{GeV}/c)^2$ ,  $\theta=21^\circ$ , long target; (d)  $Q^2=5.0$   $(\text{GeV}/c)^2$ ,  $\theta=21^\circ$ , short target, 2.52% radiator; (e)  $Q^2=5.0$   $(\text{GeV}/c)^2$ ,  $\theta=21^\circ$ , short target, no external radiator; (f)  $Q^2=5.0$   $(\text{GeV}/c)^2$ ,  $\theta=25^\circ$ , long target; (g)  $Q^2=5.0$   $(\text{GeV}/c)^2$ ,  $\theta=33^\circ$ , long target; (h)  $Q^2=7.3$   $(\text{GeV}/c)^2$ ,  $\theta=21^\circ$ , long target; (i)  $Q^2=9.6$   $(\text{GeV}/c)^2$ ,  $\theta=21^\circ$ , long target.

corrected cross section on the assumed value of the cutoff in scattered energy  $E'$  used in these calculations, as translated to a cutoff in missing mass  $W^2$ . The  $C(W_{\text{cut}}^2)/C(W_{\text{cut0}}^2)$  is the ratio of the radiatively corrected number of counts summed to different values of the radiative tails. The ratio falls with decreasing  $W^2$  to the left of the nominal cutoff  $W_{\text{cut0}}^2$  due to the finite missing mass resolution of the spectrometer, and rises to the right of  $W_{\text{cut0}}^2$  due to the onset of pion production. The lower limit to the range of allowable choices of  $W_{\text{cut0}}^2$  was set by the intrinsic resolution of the apparatus. The threshold for pion production restricted the maximum choice of the cutoff to be below  $W^2=1.17$  (GeV)<sup>2</sup> by an amount equivalent to the  $W^2$  resolution. The cutoff was chosen to be at the upper edge of a  $W^2$  bin such that  $W_{\text{cut0}}^2$  was as close as possible to, but did not exceed, the value 1.10 (GeV)<sup>2</sup>. Varying the choice of the nominal cutoff in the range  $1.05 \leq W_{\text{cut0}}^2 \leq 1.15$  would produce an effect on the final elastic cross sections of less than  $\pm 1\%$ .

#### IV. ELASTIC CROSS SECTIONS AND EXTRACTION OF $G_M^p$ AND $F_1^p$

This section describes the procedures used to calculate the final elastic cross sections from the data and the extraction of the proton form factors from these data.

##### A. Steps in the calculation of the cross section

The following steps were taken to calculate the elastic cross section.

(1) Events which passed the cuts described in the previous section were binned into a two-dimensional ( $W^2, \theta$ ) histogram where  $W^2 \equiv M_p^2 + 2M_p(E - E') - Q^2$ . A statistical uncertainty  $\Delta N(W^2, \theta) \equiv [N(W^2, \theta)]^{1/2}$  was assigned to each bin.

(2) If the data were taken with the short target, the contribution to the counting rate from the end caps was subtracted using data taken at the same kinematics with the short empty target, with appropriate propagation of statistical uncertainties. If the data were taken with the long target, an examination of the kinematic region  $W^2 \ll M_p^2$  was made to verify that backgrounds from the long target walls and end caps were negligible.

(3) The variation in counting rate due to acceptance effects was removed from the data using the formula

$$\begin{aligned} N_{\text{corr}}(W^2, \theta) &= \frac{N(W^2, \theta)}{A(\delta, \theta)}, \\ \Delta N_{\text{corr}}(W^2, \theta) &= \frac{\Delta N(W^2, \theta)}{A(\delta, \theta)}, \end{aligned} \quad (14)$$

where the value of  $\delta$  was calculated from the kinematics at the center of each ( $W^2, \theta$ ) bin.

(4) The cross section varied considerably over the range of polar angle  $\theta$  accepted by the spectrometer. This variation was removed by multiplying  $N_{\text{corr}}(W^2, \theta)$  by a factor of  $\sigma_{\text{elas}}(E_0, \theta_0)/\sigma_{\text{elas}}(E_0, \theta)$  at each value of  $\theta$ , where  $\sigma_{\text{elas}}$  was the value of a model for the elastic cross section determined iteratively from previous data and from the results of early versions of the analysis of this experiment. The uncertainty  $\Delta N_{\text{corr}}(W^2, \theta)$  was multiplied by the

same factor. Removing the  $\theta$  dependence of the cross section in this manner allowed the final cross section for each measurement to be reported at the central kinematic coordinate  $\theta_0$  of the spectrometer after summing over the  $\theta$  acceptance.

(5) A weighted sum was then formed over  $\theta$  to yield a one-dimensional histogram of acceptance-corrected counts versus the missing mass squared, according to the formula

$$\begin{aligned} \bar{N}(W^2) &= \frac{n}{f} \sum_i f_i N_{\text{corr}}(W^2, \theta_i), \\ \Delta \bar{N}(W^2) &= \frac{n}{f} \left[ \sum_i [f_i \Delta N_{\text{corr}}(W^2, \theta_i)]^2 \right]^{1/2}, \end{aligned} \quad (15)$$

where  $n$  is the total number of  $\theta$  bins within the spectrometer acceptance limits  $\Delta\theta_{\text{tot}}$ ,  $f_i$  is the weight for each bin, and  $f \equiv \sum_i f_i$ . Because the counting rates were very low for most of this experiment, the usual statistical procedure of defining the weights as the inverse-squared statistical uncertainty for each bin could not be used. Instead, the model cross sections were used to define the weight as

$$f_i = \frac{A(\delta, \theta_i) \sigma_{\text{elas}}(E_0, \theta_i)}{A(0, 0) \sigma_{\text{elas}}(E_0, \theta_0)}, \quad (16)$$

where  $\delta$  was calculated from  $E_0$  and  $W^2$  for each missing mass bin and  $\sigma_{\text{elas}}(E_0, \theta_i)$  was determined using preliminary values of the form factors. The weights defined in this way were distributed in the same way as if they had been determined from a very large number of counts, and did not have the difficulties inherent in the statistical definition when dealing with a small number of counts per bin.

Figure 19 compares missing mass histograms for the raw data points at the highest and lowest values of  $Q^2$  with the expected response of the apparatus as determined by a Monte Carlo simulation. Final missing mass histograms after the application of all corrections are shown in Fig. 20. As can be seen in these figures, the elastic peak was clearly discernible at each kinematic point. The elastic peak width was dominated by the energy spread of the incident beam ( $\Delta E_0/E_0$ ). The data shown in Fig. 19(a) were taken during a single short run and are consistent with an incident energy spread  $\Delta E_0/E_0 \approx \pm 0.13\%$ , although the energy-defining slits were set to allow  $\pm 0.2\%$ . For data taken in many runs spread over a longer duration, such as those shown in Fig. 19(b), the width of the elastic peak is consistent with the full range of  $\Delta E_0/E_0$  allowed by the slits.

(6) The elastic cross section for each measurement was obtained by summing all counts in the range of the missing mass squared between 0.7 and  $W_{\text{cut0}}^2$  (GeV/ $c$ )<sup>2</sup> to yield

$$N_{\text{peak}} \equiv \sum_{W^2=0.7}^{W_{\text{cut0}}^2} \bar{N}(W^2), \quad (17)$$

where the cutoff  $W_{\text{cut0}}^2$  was chosen as described in the previous section. This value for  $N_{\text{peak}}$  was divided by the

incident beam charge  $Q$ , the number of target protons  $n_p$ , the solid angle  $\Delta\Omega = (\Delta\theta)_{\text{tot}}(\Delta\phi)_{\text{tot}}\sin\theta_0$ , the elastic radiative corrections  $C_R$  consistent with a given value of  $W_{\text{cut0}}^2$ , electronic and trigger live time corrections  $C_E$  and  $C_T$ , and corrections for the efficiencies of the detectors and software cuts  $\epsilon_{\text{CC}}$ ,  $\epsilon_{\text{TA}}$ ,  $\epsilon_{\text{CP}}$ , and  $\epsilon_{\text{WC}}$  for the Čerenkov discriminator, TA discriminator, CC+PR combination, and wire chamber efficiency, respectively. The final cross-section formula was

$$\frac{d\sigma}{d\Omega} = \frac{N_{\text{peak}}}{n_p Q C_R C_E C_T \epsilon_{\text{tot}} \Delta\Omega}, \quad (18)$$

where  $\epsilon_{\text{tot}} \equiv \epsilon_{\text{CC}}\epsilon_{\text{TA}}\epsilon_{\text{CP}}\epsilon_{\text{WC}}$  and  $n_p = N_A \rho L_V / 1.0079$ ;  $N_A$  is Avogadro's number,  $\rho$  was the target density,  $L_V$  was the visible target length, and the factor of 1.0079 is the atomic weight of hydrogen in atomic mass units. For the short target  $L_V = L$  the full length, and for the long target the visible fraction is  $L_V = FL$ , where  $F$  is determined in Eq. (13). A check was made to verify that the counting rate in the kinematically forbidden region of  $W^2$  below the cut value of 0.7 (GeV/c)<sup>2</sup> was negligible.

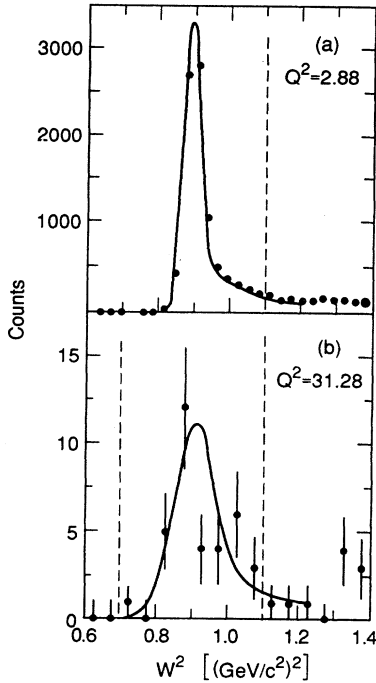


FIG. 19. Histograms of raw counts vs the missing mass squared at the highest and lowest values of  $Q^2$  in this experiment. (a)  $Q^2 = 2.883$  (GeV/c)<sup>2</sup>. (b)  $Q^2 = 31.28$  (GeV/c)<sup>2</sup>. The curves show the expected resolution of the apparatus for each case, as determined from a Monte Carlo simulation of the experiment, including acceptance and radiative effects, but neglecting inelastic reactions. The data in each case show a clear peak with no significant background in the kinematically forbidden region of  $W^2$  below the peak. The elastic radiative tail is visible above the peak. The data depart from the Monte Carlo curve near the threshold for pion production [ $W^2 = 1.17$  (GeV/c)<sup>2</sup>], as expected. The counts between the dashed vertical lines were summed to obtain the cross sections.

The cross-section results for all the different beam, target, and spectrometer settings are given in the Appendix. A summary of results containing the averages of cross sections measured at nearly the same kinematic points is given in Table V. The averaging process included small extrapolations to a common value of  $Q^2$  for measurements taken with slightly different values of beam energy. Systematic uncertainties in the cross-section results are discussed in a separate section below.

The final results for E136 presented in this paper supersede the preliminary results presented in Ref. [9]. The new cross-section values tend in general to be a few percent higher than those from the previous analysis. These differences are mainly due to refinements in the calculation of the elastic radiative corrections [22] and modifications to the acceptance [21].

## B. Extraction of $G_M^p$ and $F_2^p$

Table VI gives values of the proton magnetic form factor  $G_M^p$  extracted from the data in Table V, assuming that the form factor scaling relation  $G_E^p = G_M^p / \mu_p$  observed at

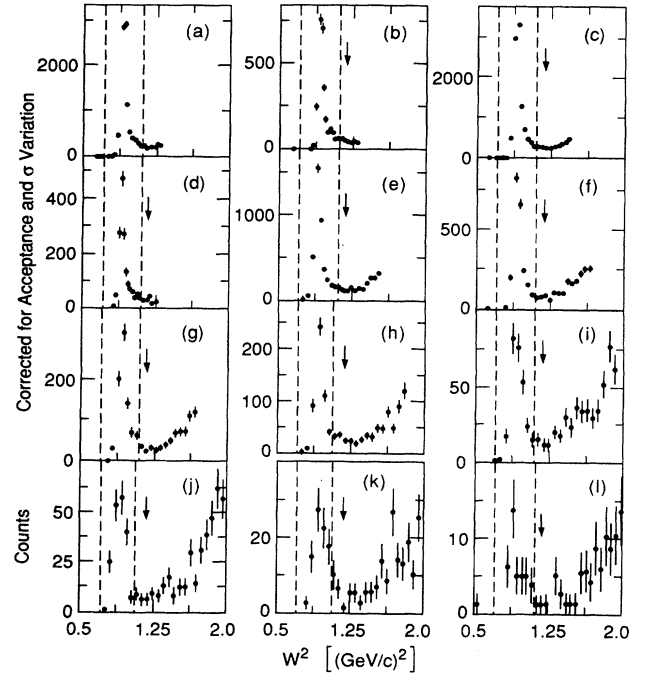


FIG. 20. Histograms of counts vs the missing mass squared corrected for the acceptance and summed over  $\Delta\theta_{\text{tot}}$  as in Eq. (15). (a)  $Q^2 = 2.9$  (GeV/c)<sup>2</sup>,  $\theta = 21^\circ$ ; (b)  $Q^2 = 3.6$  (GeV/c)<sup>2</sup>,  $\theta = 25^\circ$ ; (c)  $Q^2 = 5.0$  (GeV/c)<sup>2</sup>,  $\theta = 21^\circ$ ; (d)  $Q^2 = 5.0$  (GeV/c)<sup>2</sup>,  $\theta = 33^\circ$ ; (e)  $Q^2 = 7.3$  (GeV/c)<sup>2</sup>,  $\theta = 21^\circ$ ; (f)  $Q^2 = 9.7$  (GeV/c)<sup>2</sup>,  $\theta = 21^\circ$ ; (g)  $Q^2 = 11.9$  (GeV/c)<sup>2</sup>,  $\theta = 21^\circ$ ; (h)  $Q^2 = 15.7$  (GeV/c)<sup>2</sup>,  $\theta = 21^\circ$ ; (i)  $Q^2 = 19.4$  (GeV/c)<sup>2</sup>,  $\theta = 21^\circ$ ; (j)  $Q^2 = 23.2$  (GeV/c)<sup>2</sup>,  $\theta = 21^\circ$ ; (k)  $Q^2 = 27.0$  (GeV/c)<sup>2</sup>,  $\theta = 25^\circ$ ; (l)  $Q^2 = 31.2$  (GeV/c)<sup>2</sup>,  $\theta = 33^\circ$ . The threshold for pion production is marked by an arrow on these plots. Data points between the dashed lines were summed to yield the total counts  $N_{\text{peak}}$ . Counting rates in the kinematically forbidden region of  $W^2$  below the lower cut value of 0.7 (GeV/c)<sup>2</sup> were negligible.

TABLE V. Kinematic settings and elastic electron-proton cross sections. The cross-section results are the average of individual results given in the Appendix obtained from data taken under various beam and target conditions in parts I and II. Results at slightly different kinematics have been extrapolated to common values of  $E_0$  and  $Q^2$ . The statistical and total systematic errors described in the text are listed separately.

$E$ (GeV)	$E'$ (GeV)	$\theta$ (deg)	$Q^2$ [(GeV/c) <sup>2</sup> ]	$d\sigma/d\Omega \pm \text{stat} \pm \text{syst}$ (nb/sr)
5.464	3.939	21.01	2.862	$0.802 \pm 0.009 \pm 0.029$
5.464	3.534	25.01	3.621	$0.193 \pm 0.004 \pm 0.007$
7.632	4.953	21.01	5.027	$(6.93 \pm 0.03 \pm 0.25) \times 10^{-2}$
6.657	3.998	25.01	4.991	$(4.55 \pm 0.08 \pm 0.16) \times 10^{-2}$
5.499	2.826	33.01	5.017	$(2.04 \pm 0.03 \pm 0.07) \times 10^{-2}$
9.606	5.716	21.01	7.300	$(1.09 \pm 0.02 \pm 0.04) \times 10^{-2}$
11.45	6.323	21.01	9.629	$(2.51 \pm 0.06 \pm 0.09) \times 10^{-3}$
13.21	6.824	21.01	11.99	$(8.08 \pm 0.21 \pm 0.29) \times 10^{-4}$
15.84	7.463	21.01	15.72	$(1.79 \pm 0.09 \pm 0.06) \times 10^{-4}$
18.36	7.979	21.01	19.47	$(4.67 \pm 0.32 \pm 0.17) \times 10^{-5}$
20.79	8.407	21.01	23.24	$(1.82 \pm 0.15 \pm 0.07) \times 10^{-5}$
21.18	6.796	25.01	26.99	$(4.51 \pm 0.50 \pm 0.16) \times 10^{-6}$
21.19	4.561	33.01	31.20	$(8.6 \pm 1.5 \pm 0.3) \times 10^{-7}$

low-momentum transfer in other experiments [1–3] continues to hold at high-momentum transfer. Table VII gives the results for extracted values of the Dirac form factor  $F_1^p$  under the same assumption. Because the cross section is proportional to the squares of the form factors, the relative uncertainties in  $G_M^p$  and  $F_1^p$  as listed in Tables VI and VII are half of those in the cross section.

As seen from these tables, a larger fraction of the cross section is attributable to  $G_M^p$  than is attributed to  $F_1^p$ . Hence, the extraction of  $F_1^p$  is more sensitive to the validity of form factor scaling than  $G_M^p$ . The results for  $G_M^p/\mu_p$  and  $F_1^p$  are plotted in Figs. 21 and 22. As discussed in the next section, naive dimensional counting based on the idea that two gluons must connect the three quarks predicts the onset of a  $1/Q^4$  falloff of  $F_1^p$ . The results have thus been scaled by  $Q^4$  in these graphs. The

TABLE VI. Extracted values of  $G_M^p$  assuming  $G_E^p = G_M^p/\mu_p$ . Also listed is the fraction of the cross section due to  $G_M^p$ . The statistical and total systematic errors described in the text are listed separately.

$Q^2$ [(GeV/c) <sup>2</sup> ]	$\theta$ (deg)	Percent of $\sigma$ due to $G_M^p$	$Q^4 G_M^p/\mu_p \pm \text{stat} \pm \text{syst}$ [(GeV/c) <sup>4</sup> ]
2.862	21.01	87.7	$0.331 \pm 0.002 \pm 0.006$
3.621	25.01	90.6	$0.361 \pm 0.004 \pm 0.007$
5.027	21.01	92.9	$0.390 \pm 0.001 \pm 0.007$
4.991	25.01	93.2	$0.391 \pm 0.003 \pm 0.007$
5.017	33.01	94.1	$0.387 \pm 0.003 \pm 0.007$
7.300	21.01	95.1	$0.397 \pm 0.004 \pm 0.007$
9.629	21.01	96.4	$0.390 \pm 0.005 \pm 0.007$
11.99	21.01	97.2	$0.392 \pm 0.005 \pm 0.007$
15.72	21.01	98.0	$0.378 \pm 0.009 \pm 0.007$
19.47	21.01	98.4	$0.343 \pm 0.012 \pm 0.006$
23.24	21.01	98.7	$0.346 \pm 0.014 \pm 0.006$
26.99	25.01	99.1	$0.339 \pm 0.020 \pm 0.006$
31.20	33.01	99.5	$0.347 \pm 0.031 \pm 0.007$

TABLE VII. Extracted values of  $F_1^p$  assuming  $G_E^p = G_M^p/\mu_p$ . Also listed is the fraction of the cross section due to  $F_1^p$ . The statistical and total systematic errors described in the text are listed separately.

$Q^2$ [(GeV/c) <sup>2</sup> ]	$\theta$ (deg)	Percent of $\sigma$ due to $F_1^p$	$Q^4 F_1^p \pm \text{stat} \pm \text{syst}$ [(GeV/c) <sup>4</sup> ]
2.862	21.01	80.2	$0.597 \pm 0.004 \pm 0.011$
3.621	25.01	82.0	$0.688 \pm 0.007 \pm 0.013$
5.027	21.01	84.8	$0.800 \pm 0.002 \pm 0.015$
4.991	25.01	84.8	$0.801 \pm 0.007 \pm 0.015$
5.017	33.01	85.2	$0.795 \pm 0.006 \pm 0.015$
7.300	21.01	88.1	$0.878 \pm 0.008 \pm 0.016$
9.629	21.01	90.4	$0.902 \pm 0.011 \pm 0.017$
11.99	21.01	92.1	$0.935 \pm 0.013 \pm 0.017$
15.72	21.01	93.9	$0.931 \pm 0.023 \pm 0.017$
19.47	21.01	95.2	$0.866 \pm 0.030 \pm 0.016$
23.24	21.01	96.0	$0.885 \pm 0.036 \pm 0.016$
26.99	25.01	97.0	$0.878 \pm 0.053 \pm 0.016$
31.20	33.01	98.1	$0.91 \pm 0.08 \pm 0.02$

slope of the data with  $Q^2$  is greater for  $G_M^p$  than for  $F_1^p$  under the assumption of form factor scaling, but the dependence of each of these quantities with  $Q^2$  is qualitatively similar since  $F_1^p$  is the dominant contribution to  $G_M^p$  under this assumption. The data agree with previous measurements at low  $Q^2$ , reaching a broad peak near  $Q^2=8$  (GeV/c)<sup>2</sup>, then decrease with increasing  $Q^2$ . A straight-line fit to our data for  $Q^4 G_M^p$  between  $Q^2=12.0$  (GeV/c)<sup>2</sup> and  $Q^2=31.3$  (GeV/c)<sup>2</sup> has a slope of  $(-3.6 \pm 1.0) \times 10^{-3}$  (GeV/c)<sup>2</sup>. For  $Q^4 F_1^p$ , the corresponding slope is  $(-0.5 \pm 0.3) \times 10^{-3}$  (GeV/c)<sup>2</sup>. The error is the combined statistical and systematic errors. Above  $Q^2=19$  (GeV/c)<sup>2</sup>, however, both  $Q^4 F_1^p$  and  $Q^4 G_M^p$

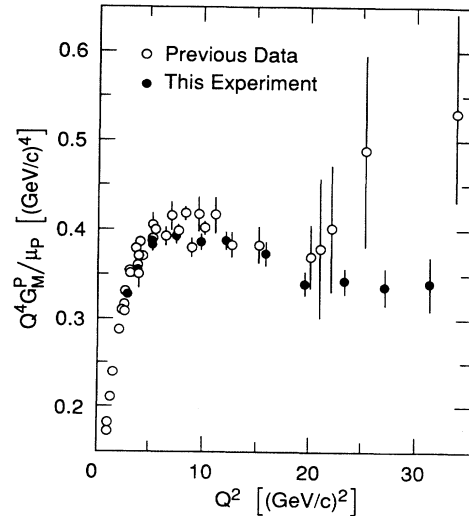


FIG. 21. Extracted values of  $Q^4 G_M^p/\mu_p$  vs  $Q^2$  assuming  $G_E^p = G_M^p/\mu_p$ . Open circles show previous data as given in Refs. [1] and [2]. Solid circles show the results of this experiment. The errors are the combined statistical and total systematic error added in quadrature.

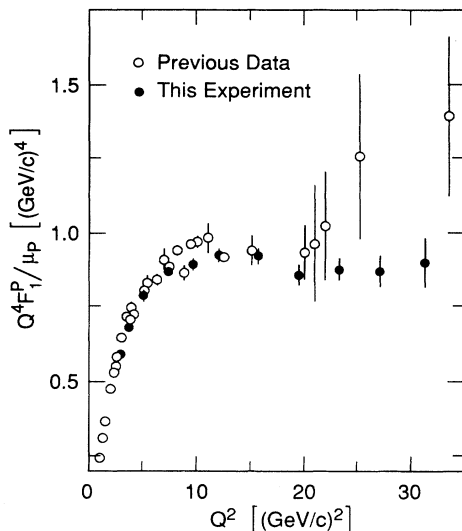


FIG. 22. Extracted values of  $Q^4 F_1^p$  vs  $Q^2$ . The extraction of the proton Dirac form factor  $F_1^p$  depends more heavily at low-momentum transfer on the assumption of form factor scaling than does the extraction of  $G_M^p$ . Form factor scaling has not yet been tested above  $Q^2=7$  (GeV/c) $^2$ . The errors are the combined statistical and total systematic uncertainties added in quadrature.

appear to be roughly independent of  $Q^2$  within the overall uncertainties of this experiment. Sources of systematic uncertainty in the cross section and form factor results are discussed in the next section.

### C. Systematic uncertainties

Systematic effects could influence the cross-section measurements due to the sources summarized below. When combined in quadrature these contributions produce total systematic uncertainties of approximately  $\pm 3.6\%$ .

#### 1. Point to point uncertainties

(a) *Incident energy.* The absolute calibration of the beam energy was not checked during this experiment. Previous experiments [1,2] using the same beam transport line have cited an overall calibration uncertainty of  $\pm 0.1\%$ . Recent calibrations [3,22] using elastic scattering measured an overall calibration uncertainty of  $0.07\%$ . The stability of the beam transport system was monitored continuously during the experiment to better than  $0.1\%$  by measuring the field in a magnet in series with the  $A$ -bend magnets. The energy spread of the incident beam was limited by slits in the transport system to be typically less than  $\pm 0.2\%$ . Observations of the width of the elastic peak showed that it was possible for the intrinsic energy spread of the beam to be smaller than the slit limits for short periods during individual runs. Deviations in the centroid of the energy spectrum were thus small compared to overall calibration uncertainties. A total uncertainty in incident beam energy of  $\Delta E_0/E_0 = \pm 0.12\%$  was assigned. At fixed  $\theta$ , the elastic cross section varies

roughly as  $E^{-8}$  to  $E^{-9}$  depending on kinematics. The resulting uncertainty on cross-section measurements was about  $\pm 1.1\%$ .

(b) *Final energy.* The central momentum of the 8-GeV/c spectrometer was controlled to within  $\pm 0.05\%$  during the course of the experiment. The calibration of spectrometer momentum was checked relative to the incident beam energy and spectrometer angle, using elastic scattering at low-momentum transfer. This check was made by comparing the location of the missing mass peak with results of a Monte Carlo simulation that included the effects of multiple scattering, spectrometer acceptance, and elastic radiative corrections. The results indicated less than  $\pm 0.1\%$  error in spectrometer momentum calibration. The resulting uncertainty on cross sections was negligible since we integrated over almost the entire elastic peak.

(c) *Scattering angle.* The spectrometer angle could be set to a precision of  $\pm 0.002^\circ$ , and was known to an overall accuracy of  $\pm 0.005^\circ$  by direct surveying. The cross section varied as  $1/\theta^{10}$  to  $1/\theta^{12}$  depending on  $Q^2$ . The measurements at the highest two values of  $Q^2$  were taken at wider angles than were the majority of the data, and were less sensitive to absolute errors in  $\theta$ . The scattering angle was also smeared slightly by the effects of multiple scattering in the target and detectors. The overall effect from uncertainty in  $\theta$  was an uncertainty of roughly  $\pm 0.5\%$  in the cross section.

(d) *Incident beam angle.* The alignment of the incident beam was measured by observing beam spots on two ZnS screens upstream of the target. The screens were normally out of the beam and were inserted between data runs to check the alignment. In this manner, the incident beam angle was controlled to within  $\pm 0.2$  mrad, producing an uncertainty in cross sections of typically  $\pm 1.0\%$ .

(e) *Beam charge.* The beam charge was measured by inductive pickup using two independent toroidal charge monitors. Each toroid was instrumented with two different sets of readout electronics. The signals were calibrated to within  $\pm 0.1\%$  by sending a known charge through small test coils. Typical differences between measurements of the same beam current in the two toroids, after correction for calibration, were within  $\pm 0.2\%$ . The calibrations were repeated every few hours. The zero levels of the readout electronics were adjusted when necessary. Changes in the gain of each system were usually within  $\pm 0.5\%$  between calibrations. In a previous experiment [26] the toroids were compared with a Faraday cup, and agreed to within  $0.5\%$ . Based on these considerations, a total uncertainty of  $\pm 0.5\%$  was assigned to the cross-section measurements to cover uncertainties in the measurement of the beam charge.

(f) *Target density.* As discussed earlier, local beam-induced density changes were observed in the long target during the first part of the experiment that gave corrections to the cross sections of  $(6 \pm 2)\%$ . Approximately 40% of the data at  $Q^2=31.3$  (GeV/c) $^2$  were taken under these conditions. During the second part of the experiment, improvements in the hydrogen flow reduced local density changes to a negligible level. The resulting systematic uncertainty in target density is  $\pm 1.0\%$  for the

combined  $Q^2=31.3$  (GeV/c)<sup>2</sup> data sets, and  $\pm 0.5\%$  for all other data.

(g) *Radiative corrections.* The expected level of confidence in the theoretical approach to radiative corrections presented in Refs. [25] and [22] should be on the order of 1%, since terms of order  $\alpha^2$  and higher were neglected. Based on these considerations and on observed stability of the cross section for different choices of the cutoff  $W_0$  in the missing mass, and the agreement between the various cross-checks of radiative correction-related effects as discussed earlier, we assign a systematic uncertainty of  $\pm 1.0\%$  to the cross sections due to uncertainties in radiative corrections.

### 2. Overall uncertainties

Although it is difficult in some cases to draw clear distinctions, the factors summarized above in general could vary on a short term basis, and so be different for each  $Q^2$  data point. The following sources of systematic uncertainty would be the same for each data point, and changes in these factors would affect all data by roughly the same amount.

(a) *Optics.* From our examination of the results of both historical optics data and our new measurements, we conclude that the overall uncertainty in acceptance due to uncertainties in optical coefficients is less than  $\pm 2\%$ .

(b) *Acceptance normalization between long and short targets.* The relative normalization of acceptance between the long and short targets was determined using data from inelastic scattering, and checked by using elastic scattering. An average difference of  $(-1.9 \pm 1.4)\%$  was observed between elastic cross sections measured under identical conditions with the two targets. We assign a systematic uncertainty of  $\pm 2.0\%$  to the cross sections to cover uncertainties in relative acceptance normalization.

(c) *Detector efficiencies and dead time.* Uncertainties in determination of detector efficiencies and dead time can contribute in a systematic way to uncertainties in the cross sections. Efficiencies of individual detector elements were determined to within  $\pm 0.5\%$  by a variety of methods. Dead time in the electronics and trigger as measured by scalers was generally less than a few percent, so the correction should be reliable to a fraction of a percent. The overall systematic effect on cross sections due to these considerations is less than  $\pm 1\%$ .

### 3. Total systematic uncertainty

The above contributions to the systematic uncertainty are summarized in Table VIII. The dominant contributions are from uncertainties in acceptance, from uncertainties in optics coefficients, and from relative normalization of the long and short targets. Other important contributions come from uncertainties in incident beam angle and energy, radiative corrections, and detector efficiencies. The total systematic uncertainty in  $d\sigma/d\Omega$  is less than  $\pm 3.6\%$ .

TABLE VIII. Sources of systematic uncertainty in  $d\sigma/d\Omega$ .

Source	$\Delta\sigma/\sigma$ (%)
Point to point uncertainties	
Incident energy	$\leq 1.1$
Scattering angle	0.5
Incident beam angle	1.0
Target density	0.5 <sup>a</sup>
Beam charge	0.5
Radiative corrections	1.0
Sum in quadrature	2.0 (2.2) <sup>a</sup>
Overall uncertainties	
Optics	2.0
Acceptance normalization	2.0
Detector efficiencies	1.0
Sum in quadrature	3.0
Total	3.6 (3.7) <sup>a</sup>

<sup>a</sup>This uncertainty applies to the data point at  $Q^2=31$  (GeV/c)<sup>2</sup> from target density variations due to beam heating in E136 I.

## V. COMPARISON WITH THEORY

In the 1960s, experiments [27] at CEA, DESY, Stanford, and SLAC first showed the simple dipole behavior and scaling behavior

$$G_M^p \approx \mu_p (1 + Q^2/0.71)^{-2}, \quad (19)$$

$$G_E^p \approx G_M^p / \mu_p,$$

of the form factors of the proton, where  $Q^2$  is in (GeV/c)<sup>2</sup> and  $\mu_p = 2.793 \dots$  is the proton magnetic moment. These relations were later shown to hold up to values of four-momentum transfer squared  $Q^2$  of a few (GeV/c)<sup>2</sup>, and indicated a root-mean-square charge radius for the proton of about 0.8 fm. Such data showed that the proton was an extended object. In the years that followed, quantum chromodynamics (QCD) was developed as the most convincing present theory for the interactions between these quarks, formulated in terms of the exchange of colored vector gluons.

At sufficiently high values of  $Q^2$ , the running strong-coupling constant  $\alpha_s(Q^2)$  is expected to become small enough, due to the property of asymptotic freedom, to allow the use of perturbation theory to simplify QCD calculations. However, there is considerable controversy as to how large a value of  $Q^2$  is sufficient for perturbative QCD (PQCD) to be applicable. In the case of elastic electron nucleon scattering, the estimates range from [4,28]  $\sim 8$  (GeV/c)<sup>2</sup> to [29]  $\sim 100$  (GeV/c)<sup>2</sup>. As we will see below, both perturbative and nonperturbative QCD calculations, as well as other models, are able to approximate the experimental results, thus leaving the debate over PQCD unsettled.

### A. Comparison with dimensional scaling

Exclusive processes such as elastic electron-proton scattering are predicted to have a simple dimensional

scaling [4,28] at large enough  $Q^2$ . In this case, only the valence quark states are important, and a rough idea of the  $Q^2$  dependence can be gained by simply counting the number of quark-gluon vertices. Elastic form factors, for example, should scale asymptotically as  $(Q^2)^{-(n-1)}$ , where  $n$  is the number of valence quarks participating in the leading twist interaction. For  $e$ - $p$  elastic scattering,  $n=3$ , and thus the leading twist contributions to the structure functions should behave as  $\sim Q^{-4}$ . Since both  $G_M^p$  and  $F_1^p$  are dominated by the leading twist terms,  $Q^4 G_M^p \propto Q^4 F_1^p \sim \text{const.}$  The difference between  $G_M^p$  and  $F_1^p$  is of higher order in  $Q^2$ . The results in Figs. 21 and 22 are in rough agreement with dimensional scaling for  $Q^2 \geq 5$  (GeV/c) $^2$ . Above  $Q^2 \sim 12$  (GeV/c) $^2$ , both  $Q^4 G_M^p$  and  $Q^4 F_1^p$  seem to decrease with increasing  $Q^2$ . Within the context of dimensional scaling, this might mean that additional contributions, such as those from perturbative QCD, are required.

## B. Comparison with QCD predictions

### 1. Perturbative calculations

Perturbative QCD [4] predicts calculable logarithmic departures from the  $Q^2$  dependence of exclusive amplitudes given by the simple dimensional scaling law. It is used to calculate the leading twist portion of  $F_1^p$  to leading order in  $\alpha_s$  by factorizing the QCD expression into a convolution of three amplitudes:

$$G_M^p \propto F_1^p(Q^2) \propto \int [dx] [dy] \Phi^*(y, \bar{Q}_y^2) T_H(x, y, Q^2) \Phi(x, \bar{Q}_x^2), \quad (20)$$

where  $[dx] \equiv dx_1 dx_2 dx_3 \delta(1 - \sum_i x_i)$ ,  $x_i$  is the momentum fraction of the  $i$ th valence quark,  $\Phi(x)$  is the probability amplitude for the distribution of longitudinal momentum of the quarks in the initial-state nucleon ( $y$  corresponds to the final-state quarks), and  $T_H$  is the two-gluon exchange hard scattering amplitude. The integral is roughly proportional to  $\alpha_s^2$  due to the two-gluon exchange. The earliest efforts [4,7] used unrealistic symmetric distribution amplitudes and required a large multiplicative factor to normalize the results to the data at  $Q^2 \approx 10$  (GeV/c) $^2$ . The curve from Brodsky and Lepage [4] normalized to agree with the new data at  $Q^2 \approx 10$  (GeV/c) $^2$ , labeled BL in Figs. 23 and 24, matches the shape of the data using  $\Lambda = 100$  MeV. The normalization is very sensitive to the functional form assumed for the distribution amplitude, which contains the nonperturbative dynamics of the proton structure. To obtain more realistic results, QCD sum rules [30–40] have been used to estimate the moments of the nucleon distribution amplitudes. The proton distribution amplitude evaluated by this method differs dramatically from both the asymptotic form and from the static form used in early calculations. Chernyak and Zhitnitsky [31] (CZ) proposed a model form for the nucleon distribution amplitude which satisfies the sum rules and in which the momentum balance of the valence quarks in the proton is quite asymmetric. Their result, la-

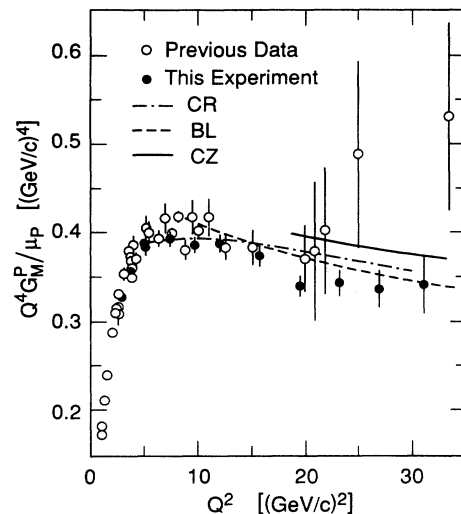


FIG. 23. Extracted values of  $Q^4 G_M^p / \mu_p$  vs  $Q^2$  compared with various perturbative QCD predictions. The curves show the predictions of Refs. [4] (BL) and [31] (CZ) for  $\Lambda_{\text{QCD}} = 100$  MeV, and that of Ref. [8] (CR) for  $\Lambda_{\text{QCD}} = 474$  MeV. The calculation of BL was normalized to the data at  $Q^2 \approx 10$  (GeV/c) $^2$ . The errors are the combined statistical and total systematic uncertainties added in quadrature.

beled CZ in Figs. 23 and 24, is  $\sim 10\%$  higher than the data, and has the correct shape.

Gari and Stefanis [32] (GS) proposed an alternative model which satisfies only some of the sum rules, and in which the momentum balance was different than that of Chernyak and Zhitnitsky but still quite asymmetric. This distribution amplitude was chosen to yield neutron form factors in agreement with a simultaneous phenomenological fit to proton and neutron cross-section data in terms

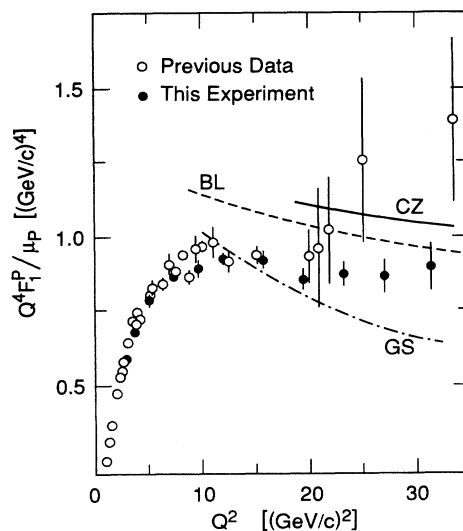


FIG. 24. Extracted values of  $Q^4 F_1^p / \mu_p$  vs  $Q^2$  compared with various QCD predictions, Refs. [4] (BL), [31] (CZ), and [32,33] (GS). The errors are the combined statistical and total systematic uncertainties added in quadrature.

of the parameters of a vector dominance model, with modifications motivated by QCD. Values of  $Q^4 F_1^p$ , calculated by Stefanis [33] using the GS distribution amplitude are labeled GS in Fig. 24. The model has approximately the same overall magnitude as the data, but falls more rapidly with  $Q^2$ . Their values of  $F_1^p$  are small which may provide a possible way to distinguish between models for the nucleon distribution amplitude. The relationships between form factors for various exclusive processes involving nucleons were further explored in Refs. [33] and [41] in which four models consistent with the QCD sum-rule restrictions are given.

Ji, Sill, and Lombard-Nelsen [42] (JSL) studied the  $Q^2$  dependence of  $F_1^p$  in more detail by evaluating the arguments of each of the factors of  $\alpha_s(Q^2)$  at the explicit values of  $Q^2$  of each of the two exchanged gluons within the integrals governing the perturbative QCD calculation. They avoided divergences caused by the limit of zero-gluon momentum by introducing a cutoff parameter [43],  $m_g$ , which is determined from the data. They obtain good agreement with the data using  $\Lambda=0.1$  GeV and either the Chernyak and Zhitnitsky [31] or Gari and Stefanis [32] distribution amplitudes both with  $m_g^2=0.3$  (GeV)<sup>2</sup> or with the King and Sachrajda [35] distribution amplitudes with  $m_g^2=0.6$  (GeV)<sup>2</sup>. A range of their predictions is shown in Fig. 25.

The curve labeled CR in Fig. 23 is from a two-loop calculation [8] of  $G_M^p(Q^2)$  by Coquereaux and de Rafael with two free variables which have been adjusted to fit the previous data. The authors state that they can calculate

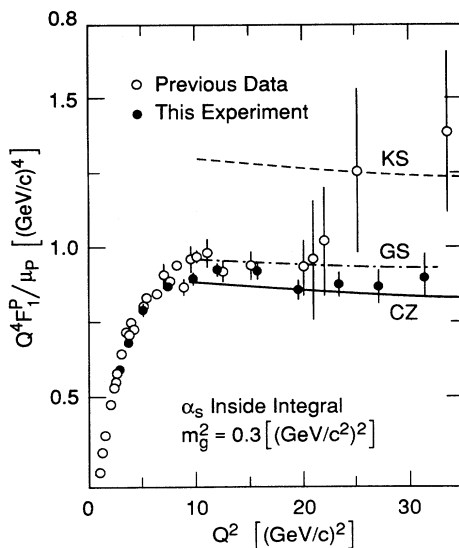


FIG. 25. Extracted values of  $Q^4 F_1^p$  compared with leading twist calculations using three different models for the distribution amplitude  $\phi(x, Q^2)$ . The models shown are Refs. [35] (KS), [32] (GS), and [31] (CZ). The arguments of the running strong-coupling constant  $\alpha_s(Q^2)$  are evaluated within the QCD integrals, as calculated in Ref. [42]. The results are shown for the values  $m_g^2=0.3$  (GeV/c<sup>2</sup>)<sup>2</sup> and  $\Lambda=0.1$  GeV/c. The errors are the combined statistical and total systematic uncertainties added in quadrature.

both the electric and magnetic form factors  $G_E^p$  and  $G_M^p$ ; we show their prediction against the data for  $G_M^p$  only and not against  $F_1^p$ .

## 2. Nonperturbative calculations

Nonperturbative methods for calculation of QCD processes have undergone rapid evolution in the past few years. Problems that were once thought to be incalculable are now being addressed using lattice gauge theory [38,44], the method of QCD sum rules [30–40], and other techniques [45,46]. In nonperturbative calculations, the form factors are evaluated by direct integration of the wave functions, rather than by separating the calculation into a set of valence quark distribution amplitudes convoluted with a “hard” piece that would be calculated perturbatively. In most nonperturbative models, the wave functions are also allowed to contain significant admixtures of nonvalence states, and even to be dominated by such contributions.

The nonperturbative calculations of Nesterenko and Radyushkin [45] for  $G_M^p$  are labeled NR in Fig. 26. They fix the parameters of the soft wave function by QCD sum rules, and use local quark-hadron duality to calculate the form factors. This calculation matches the data at low and intermediate values of  $Q^2$ , but tends to fall more steeply than the data at high  $Q^2$ . The curves labeled IL in Fig. 26 are three of the many possible soft gluon calculations of Isgur and Llewellyn-Smith [29]. They point out that soft gluon contributions are sufficient to match the data and thus perturbative QCD cannot dominate even at the highest  $Q^2$  measured so far. The assumptions of curve (g) lead to a prediction for  $G_E$  which is a factor of 2 larger than recent data [3] while model (c) is close to the  $G_E$  data.

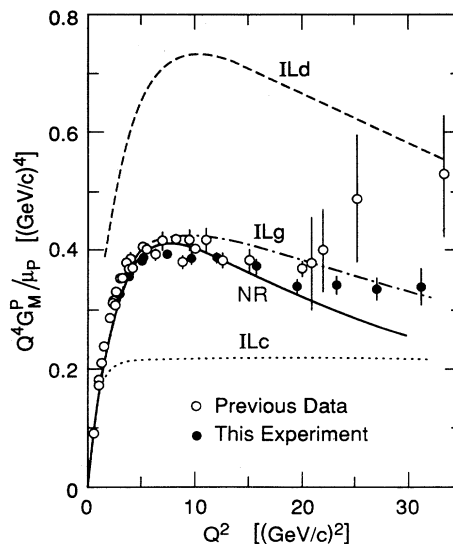


FIG. 26. Extracted values of  $Q^4 G_M^p / \mu_p$  vs  $Q^2$  compared with predictions from nonperturbative QCD. The curves show the prediction of Ref. [45] (NR) and a sample of the models of Ref. [29] (IL). The errors are the combined statistical and total systematic uncertainties added in quadrature.

A recent calculation [47] has demonstrated that distribution amplitudes required for the perturbative QCD approach can be calculated directly from hadron momentum-space wave functions. These distribution amplitudes can be adjusted to show the same general features as those calculated from QCD sum rules or lattice techniques. This calculation is especially interesting because the same momentum-space wave functions were then used to make nonperturbative calculations for the soft part of the form factors, producing results for the proton similar to those shown labeled NR in Fig. 26.

### 3. Hybrid models with perturbative QCD

Gari and Krümpelmann [48] incorporated vector meson dominance (VMD) at low  $Q^2$  and the asymptotic behavior predicted by perturbative QCD at high  $Q^2$ . Their result, shown in Fig. 27, was produced from a fit to previous data, not including the results of this experiment. Nonetheless, the fit describes the new data very well. However, notice that the experimental data were extracted under the assumption that  $G_E^p = G_M^p / \mu_p$ , which is different from the relation between proton form factors given by the fit.

Furuichi and Watanabe [49] give a theoretical justification for using VMD at low energy with PQCD at higher energy. Unsubtracted dispersion relations express the hadronic part, while superconvergence conditions are imposed to satisfy the asymptotic constraints required by PQCD. Their multiparameter fit matches the data for both neutron and proton form factors, including results from this experiment.

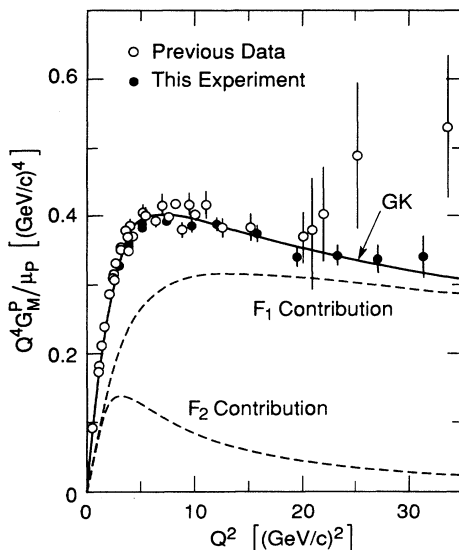


FIG. 27. Extracted values of  $Q^4 G_M^p / \mu_p$  compared with the semiphenomenological fit by Gari and Krümpelmann [48] to previous proton and neutron form factor data. Dashed lines show the contributions to  $Q^4 G_M^p / \mu_p$  of the Dirac and Pauli form factors in this model. The errors are the combined statistical and total systematic uncertainties added in quadrature.

### 4. Diquark model

The highly asymmetrical quark distribution required by the perturbative QCD models can be justified [50] within the diquark model. The highly correlated pair of quarks are a way of describing correlations in the wave function. The model of Kroll, Schurmann, and Schweiger [51] is a generalization of the hard scattering scheme for exclusive reactions. They determine the model parameters by a fit to world data including previously reported results from this experiment. The results match our data quite well.

### C. Conclusions

The results of this experiment, extracted as either  $F_1^p(Q^2)$  or  $G_M^p(Q^2)$ , show a rough agreement with dimension scaling for  $Q^2 \geq 5$   $(\text{GeV}/c)^2$ . The visible but small decrease of  $Q^4 G_M^p$  at larger  $Q^2$  is consistent with the predictions of perturbative QCD with a small value of  $\Lambda \sim 100$  MeV. However, purely PQCD models require highly asymmetrical proton distribution amplitudes to achieve the required magnitude of  $Q^4 G_M^p$ . This asymmetry is consistent with QCD sum rules and has been justified in the diquark model. However, it is far from the expected asymptotic distributions and for some authors [29] it is “nonintuitive.”

The nonperturbative calculations succeed in modeling the region  $Q^2 \leq 20$   $(\text{GeV}/c)^2$  fairly well, but some have difficulty at the high  $Q^2$  of our experiment. Various hybrid models can fit the data quite well, but the number of free parameters is not very satisfying.

It is clear that further theoretical efforts to investigate the exact normalization of the PQCD result and to improve the quality of the predictions are justified by the precision of the new data.

### ACKNOWLEDGMENTS

We wish to acknowledge the support of D. Brown, J. Mark, J. Nicol, B. Smith, R. Eisele, D. Tsang, and the rest of the SLAC staff, and valuable discussions with S. Brodsky and C. R. Ji. This work was supported in part by U.S. Department of Energy Contract No. DE-AC03-76SF00515 (SLAC), and by National Science Foundation Grants No. PHY83-40337 and No. PHY85-10549 (American University). R.M.L.-N. was supported by CNRS (French National Center for Scientific Research). J.G. was partially supported by CONICIT, Venezuela.

### APPENDIX: EXPERIMENTAL RESULTS

Table IX contains the results for each of the elastic cross-section measurements of this experiment. Where more than one result is given for a particular target at the same kinematic point, the conditions or apparatus were different for each of the measurements.

For part of the experiment, one element (TA1) of the

TABLE IX. A complete list of experimental results for elastic  $e$ - $p$  cross sections and statistical errors for each condition of data taking during E136 I and E136 II. Targets  $S$  and  $L$  refer to the short (25 cm) and long (65 cm) targets, respectively. "Counts" refer to the quantity  $N_{\text{peak}}$  defined in the text, which gives the elastically scattered electrons detected, summed over  $\theta$  and  $\delta$ , and corrected for the nonuniformity of the acceptance and variation of the cross section across the  $\theta$  acceptance of the spectrometer. "Beam" is the number of incident electrons in peta electrons ( $1Pe = 10^{15}$  electrons).  $C_R$  is the radiative correction factor.

$Q^2$ [(GeV/c) <sup>2</sup> ]	$\theta_0$ (deg)	Target	Counts	Beam		$d\sigma/d\Omega$ (nb/sr)
				(Pe)	$C_R$	
E136 I						
5.026	21.01	Short	14 230	436.7	0.642	$(7.04 \pm 0.06) \times 10^{-2}$
5.025	21.01	Short <sup>a</sup>	5834	200.6	0.575	$(7.04 \pm 0.10) \times 10^{-2}$
5.026	21.01	Short	5353	168.6	0.642	$(6.86 \pm 0.10) \times 10^{-2}$
5.024	21.01	Short <sup>b</sup>	5776	221.4	0.529	$(6.90 \pm 0.10) \times 10^{-2}$
5.017	33.01	Short	2774	271.9	0.687	$(2.05 \pm 0.04) \times 10^{-2}$
11.99	21.01	Short <sup>a</sup>	191	617.9	0.509	$(8.46 \pm 0.67) \times 10^{-4}$
11.99	21.01	Short	768	2320	0.577	$(7.99 \pm 0.33) \times 10^{-4}$
31.20	33.01	Long	15.1	24550	0.503	$(9.61 \pm 2.6) \times 10^{-7}$
E136 II						
2.862	21.01	Long	9276	12.32	0.645	$(8.02 \pm 0.09) \times 10^{-1}$
3.621	25.01	Long	2716	15.26	0.647	$(1.93 \pm 0.04) \times 10^{-1}$
4.976	21.01	Long	9907	151.7	0.607	$(7.06 \pm 0.08) \times 10^{-2}$
4.988	21.01	Short <sup>a</sup>	9588	306.1	0.596	$(7.20 \pm 0.08) \times 10^{-2}$
4.989	21.01	Short	9541	278.9	0.665	$(7.06 \pm 0.08) \times 10^{-2}$
4.991	25.01	Long	4078	98.84	0.625	$(4.55 \pm 0.08) \times 10^{-2}$
4.968	33.01	Long	1551	80.73	0.654	$(2.16 \pm 0.06) \times 10^{-2}$
4.977	33.01	Long	1385	75.78	0.654	$(2.05 \pm 0.06) \times 10^{-2}$
7.300	21.01	Long	3990	409.8	0.584	$(1.09 \pm 0.02) \times 10^{-2}$
9.629	21.01	Long	2173	1019	0.558	$(2.51 \pm 0.06) \times 10^{-3}$
11.96	21.01	Long	820	1190	0.551	$(8.17 \pm 0.31) \times 10^{-4}$
15.72	21.01	Long	495	3595	0.506	$(1.79 \pm 0.09) \times 10^{-4}$
19.47	21.01	Long	258	7348	0.492	$(4.67 \pm 0.31) \times 10^{-5}$
23.25	21.01	Long	116	8877	0.480	$(1.80 \pm 0.18) \times 10^{-5}$
23.25	21.01	Long	67.0	4973	0.480	$(1.85 \pm 0.25) \times 10^{-5}$
26.99	25.01	Long <sup>c</sup>	22.3	6673	0.481	$(5.21 \pm 1.20) \times 10^{-6}$
27.00	25.01	Long	62.6	20840	0.481	$(4.29 \pm 0.59) \times 10^{-6}$
31.18	33.01	Long <sup>c</sup>	5.03	9182	0.517	$(8.30 \pm 4.1) \times 10^{-7}$
31.19	33.01	Long	19.1	32830	0.516	$(8.05 \pm 2.0) \times 10^{-7}$

<sup>a</sup>Additional 0.0252 r.l. inserted in front of the target.

<sup>b</sup>Additional 0.0438 r.l. inserted in front of the target.

<sup>c</sup>TA1 counter not working.

total absorber section of the shower counter was not working. The data for those runs were analyzed with a restricted subset of the acceptance. Some data were taken with an extra thickness of Al radiator (listed here in

radiation lengths) inserted ahead of the target as a check on the radiative corrections procedures. A summary listing the average results at each kinematic point is given in Table V in the main text.

[1] M. D. Mestayer, SLAC-214, Ph.D. thesis, Stanford University, 1978; W. B. Atwood, SLAC-185, Ph.D. thesis, Stanford University, 1975; in *Deep Hadronic Structure and the New Particles*, Proceedings of the Summer Institute on Particle Physics, Stanford, California, 1975, edited by M. C. Zipf (SLAC Report No. SLAC-191, Stanford, 1976); G. Hohler *et al.*, Nucl. Phys. **B114**, 505 (1976); F. Borokowski *et al.*, *ibid.* **B93**, 461 (1975); Nucl. Phys. **A222**, 269 (1974); Z. Phys. A **275**, 29 (1975).

[2] P. N. Kirk *et al.*, Phys. Rev. D **8**, 63 (1973); J. Litt *et al.*, Phys. Lett. **31B**, 40 (1970); D. H. Coward *et al.*, Phys. Rev. Lett. **20**, 292 (1968), and references contained therein.

[3] P. E. Bosted *et al.*, Phys. Rev. Lett. **68**, 3841 (1992).

[4] S. J. Brodsky and G. P. Lepage, Phys. Rev. D **22**, 2157 (1980); G. P. Lepage and S. J. Brodsky, Phys. Rev. Lett. **43**, 545 (1979); **43**, 1625(E) (1979).

[5] V. L. Chernyak and A. R. Zhitnitsky, Yad. Fiz. **31**, 1053

- (1980) [Sov. J. Nucl. Phys. **31**, 544 (1980)]; V. A. Avdeenko, S. E. Korenblit, and V. L. Chernyak, *ibid.* **33**, 481 (1981) [**33**, 252 (1981)].
- [6] I. G. Aznauryan, S. V. Esaybegyan, and N. L. Ter-Isaaksan, Phys. Lett. **90B**, 151 (1980).
- [7] A. Duncan and A. H. Mueller, Phys. Lett. **90B**, 159 (1980); A. Duncan and A. H. Mueller, Phys. Rev. D **21**, 1636 (1980).
- [8] R. Coquereaux and E. de Rafael, Phys. Lett. **74B**, 105 (1978).
- [9] R. G. Arnold *et al.*, Phys. Rev. Lett. **57**, 174 (1986).
- [10] A. F. Sill, Ph.D. thesis, The American University, 1987.
- [11] R. B. Neal, *The Stanford Two-Mile Accelerator* (Benjamin, New York, 1968); SLAC Report No. SLAC-PUB-398, 1968 (unpublished). SLAC User's Handbook (unpublished), Sec. B.3.
- [12] See Kirk *et al.* [2].
- [13] R. S. Larsen and D. Horelick, in *Proceedings of the Symposium on Beam Intensity Measurement*, Daresbury, England, 1968 (Daresbury Nuclear Physics Laboratory, Daresbury, 1968), pp. 260–279.
- [14] J. Mark, in *Advances in Cryogenic Engineering* (Plenum, New York, 1984), Vol. 30.
- [15] J. Mark, in *Advances in Cryogenic Engineering* [14], Vol. 32.
- [16] P. Bosted and A. A. Rahbar, "A Proportional Wire Chamber System for the SLAC 8 GeV/c Spectrometer," Nuclear Physics at SLAC Report No. SLAC-NPAS-85-1, 1985 (unpublished).
- [17] J. G. Gomez, "Shower Counter for the SLAC 8 GeV/c Spectrometer," Nuclear Physics at SLAC Report No. SLAC-NPAS-84-1, 1984 (unpublished).
- [18] SLAC User's Handbook [11], Sec. D.3; see also Kirk *et al.* [2].
- [19] K. L. Brown, SLAC Report No. SLAC-75 Rev. 3, 1972 (unpublished); K. L. Brown, F. Rothacker, D. C. Carey, and Ch. Iselin, SLAC-Report-91, Rev. 2, 1977 (unpublished).
- [20] A. F. Sill, "Jailbar Optical Studies of the SLAC 8 GeV/c Spectrometer," Nuclear Physics at SLAC Report No. SLAC-NPAS-TN-86-1, 1986 (unpublished).
- [21] L. Andivahis *et al.*, SLAC Report No. SLAC-PUB-5753 (unpublished).
- [22] S. Dasu *et al.*, Phys. Rev. Lett. **61**, 1061 (1988); R. C. Walker, Ph.D. thesis, California Institute of Technology, 1989.
- [23] A. Bodek *et al.*, Phys. Rev. D **20**, 1471 (1979).
- [24] S. Stein *et al.*, Phys. Rev. D **12**, 1884 (1975).
- [25] L. W. Mo and Y. S. Tsai, Rev. Mod. Phys. **41**, 205 (1969).
- [26] S. Rock *et al.*, Phys. Rev. D **46**, 24 (1992).
- [27] E. B. Hughes *et al.*, Phys. Rev. **139**, B458 (1965); K. W. Chen *et al.*, *ibid.* **141**, 1267 (1966); J. R. Dunning *et al.*, *ibid.* **141**, 1286 (1966); L. H. Chan *et al.*, *ibid.* **141**, 1298 (1966); T. Janssens *et al.*, *ibid.* **142**, 922 (1966).
- [28] S. J. Brodsky and G. Farrar, Phys. Rev. D **11**, 1309 (1975); S. J. Brodsky and B. T. Chertok, *ibid.* **14**, 3003 (1976).
- [29] N. Isgur and C. Llewellyn-Smith, Phys. Rev. Lett. **52**, 1080 (1984); Phys. Lett. B **217**, 535 (1989); N. Isgur, in *Hadronic Physics in the 1990's with Multi-GeV Electrons*, Proceedings of the First European Workshop, Seillac, France, 1988, edited by B. Frois *et al.* [Nucl. Phys. **A497**, 229c (1989)].
- [30] M. A. Shifman, A. I. Vainshtein, and V. I. Zakharov, Nucl. Phys. **B147**, 385 (1979).
- [31] V. L. Chernyak and I. R. Zhitnitsky, Nucl. Phys. **B246**, 52 (1984); Phys. Rep. **112**, 173 (1984).
- [32] M. Gari and N. G. Stefanis, Phys. Lett. B **175**, 462 (1986); Phys. Rev. D **35**, 1074 (1987); Phys. Lett. B **187**, 401 (1987).
- [33] N. G. Stefanis, Phys. Rev. D **40**, 2305 (1989).
- [34] M. J. Lavelle, Nucl. Phys. **B260**, 323 (1985).
- [35] I. D. King and C. T. Sachrajda, Nucl. Phys. **B279**, 785 (1987).
- [36] C. E. Carlson and J. L. Poor, Phys. Rev. D **36**, 2070 (1987).
- [37] C. E. Carlson and F. Gross, Phys. Rev. D **36**, 2060 (1987).
- [38] G. Martinelli and C. T. Sachrajda, Phys. Lett. B **217**, 319 (1989).
- [39] A. Schäfer, Phys. Lett. B **217**, 545 (1989).
- [40] V. L. Chernyak, A. A. Ogloblin, and I. R. Zhitnitsky, Z. Phys. C **42**, 569 (1989).
- [41] C. E. Carlson, M. Gari, and N. G. Stefanis, Phys. Rev. Lett. **58**, 1308 (1987).
- [42] C. R. Ji, A. F. Sill, and R. M. Lombard-Nelsen, Phys. Rev. D **36**, 165 (1987); see also [10].
- [43] J. M. Cornwall, Phys. Rev. D **26**, 1453 (1982); in *Deeper Pathways in High Energy Physics*, Proceedings of the Orbis Scientiae, Coral Gables, Florida, 1977, edited by A. Perlmutter and L. F. Scott (Plenum, New York, 1977).
- [44] See, for example, S. Gottlieb and A. S. Kronfeld, Phys. Rev. D **33**, 227 (1986).
- [45] V. A. Nesterenko and A. V. Radyushkin, Yad. Fiz. **39**, 1287 (1984) [Sov. J. Nucl. Phys. **39**, 811 (1984)]; Phys. Lett. **128B**, 439 (1983); A. V. Radyushkin, in *Particles and Nuclei*, Proceedings of the Twelfth International Conference, Cambridge, Massachusetts, 1990, edited by J. L. Matthews *et al.* [Nucl. Phys. **A527**, 153c (1991)].
- [46] B. L. Ioffe and A. V. Smilga, Phys. Lett. **114B**, 353 (1982).
- [47] Z. Dziembowski and L. Mankiewicz, Phys. Rev. Lett. **58**, 1275 (1986); Z. Dziembowski, Phys. Rev. D **37**, 768 (1988); **37**, 2030 (1988).
- [48] M. Gari and W. Krümpelmann, Z. Phys. A **322**, 689 (1985); Phys. Lett. **141B**, 295 (1984).
- [49] S. Furuichi and K. Watanabe, Prog. Theor. Phys. **82**, 581 (1989); **83**, 565 (1990).
- [50] Z. Dziembowski and J. Franklin, Phys. Rev. D **42**, 905 (1990).
- [51] P. Kroll, M. Schurmann, and W. Schweiger, Z. Phys. A **338**, 339 (1991).

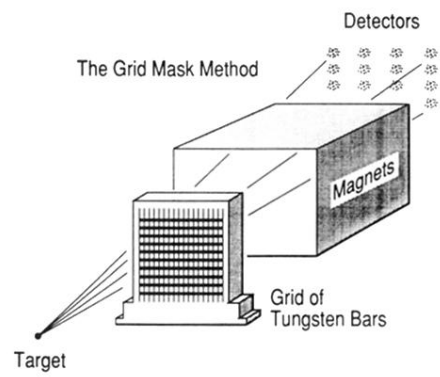


FIG. 15. Schematic representation of the grid mask method. A grid of tungsten bars is placed between a point target and the magnets of the spectrometer, forming a pattern of events in the detectors.